

# A Travel-time Path Calibration Strategy for Back-Projection of Large Earthquakes and Its Application and Validation through the Segmented Super-Shear Rupture Imaging of the 2002 Mw7.9 Denali earthquake

Shengji Wei<sup>1</sup>, Hongyu Zeng<sup>2</sup>, and Ares J Rosakis<sup>3</sup>

<sup>1</sup>Earth Observatory of Singapore

<sup>2</sup>Asian School of the Environment, Nanyang Technological University

<sup>3</sup>California Institute of Technology

November 24, 2022

## Abstract

We investigate the impact of source-side 3D velocity structure on teleseismic travel-time in back projection (BP) analysis of large earthquakes. We use travel-time data of teleseismic events recorded by the Hi-Net array to reveal how travel-time errors vary with source location. In a source area of a few hundred km, where travel-time error varies dominantly linearly, we propose a new interpolation scheme using earthquakes located around the rupture of the main-shock to calibrate the travel-time error, and validate it by relocating inland  $M > 5.0$  earthquakes in central Japan. We then apply it to image the rupture of the 2002 Denali earthquake. The calibrated BP result shows that most of the high-frequency radiators are  $< 15$  km away from the surface rupture trace. The new result reveals that the rupture started on the Susitna Glacier Fault with a speed of  $\sim 1.4$  km/s, then propagated onto the Denali Fault and accelerated to a super-shear speed approaching the crustal P-wave velocity at approximately 30 km. The location of super-shear transition and rupture speed in BP are highly consistent with that inferred from the timing and amplitude ratio of the super-shear and trailing Rayleigh pulses observed on the near fault PS-10 station. Subsequently, the rupture stagnated for  $\sim 15$  s before penetrating through the largest asperity, re-accelerated to a speed of  $\sim 5.2$  km/s and continued on the last 60 km of the Denali fault and part of Totschunda Fault. This application shows the great potential of the new BP calibration strategy to refine the rupture imaging of other mega-earthquakes.

## Hosted file

essoar.10510830.1.docx available at <https://authorea.com/users/523958/articles/603690-a-travel-time-path-calibration-strategy-for-back-projection-of-large-earthquakes-and-its-application-and-validation-through-the-segmented-super-shear-rupture-imaging-of-the-2002-mw7-9-denali-earthquake>

## Hosted file

traveltimebp\_supp.docx available at <https://authorea.com/users/523958/articles/603690-a-travel-time-path-calibration-strategy-for-back-projection-of-large-earthquakes-and-its-application-and-validation-through-the-segmented-super-shear-rupture-imaging-of-the-2002-mw7-9-denali-earthquake>

# **A Travel-time Path Calibration Strategy for Back-Projection of Large Earthquakes and Its Application and Validation through the Segmented Super-Shear Rupture Imaging of the 2002 Mw7.9 Denali earthquake**

Zeng Hongyu<sup>1</sup>, Wei Shengji<sup>1,2\*</sup>, Ares Rosakis<sup>3,4</sup>

1. Asian School of Environment, Nanyang Technological University
2. Earth Observatory of Singapore, Nanyang Technological University
3. Aerospace (GALCIT) and Mechanical Engineering, California Institute of Technology
4. Nanyang Technological University

## **Abstract**

We investigate the impact of source-side 3D velocity structure on teleseismic travel-time in back projection (BP) analysis of large earthquakes. We use travel-time data of teleseismic events recorded by the Hi-Net array to reveal how travel-time errors vary with source location. In a source area of a few hundred km, where travel-time error varies dominantly linearly, we propose a new interpolation scheme using earthquakes located around the rupture of the main-shock to calibrate the travel-time error, and validate it by relocating inland  $M > 5.0$  earthquakes in central Japan. We then apply it to image the rupture of the 2002 Denali earthquake. The calibrated BP result shows that most of the high-frequency radiators are  $< 15$  km away from the surface rupture trace. The new result reveals that the rupture started on the Susitna Glacier Fault with a speed of  $\sim 1.4$  km/s, then propagated onto the Denali Fault and accelerated to a super-shear speed approaching the crustal P-wave velocity at approximately 30 km. The location of super-shear transition and rupture speed in BP are highly consistent with that inferred from the timing and amplitude ratio of the super-shear and trailing Rayleigh pulses observed on the near fault PS-10 station. Subsequently, the rupture stagnated for  $\sim 15$  s before penetrating through the largest asperity, re-accelerated to a speed of  $\sim 5.2$  km/s and continued on the last 60 km of the Denali fault and part of Totschunda Fault. This application shows the great potential of the new BP calibration strategy to refine the rupture imaging of other mega-earthquakes.

## **Plain Language Summary**

Well-constrained rupture process of large earthquakes are critical for understanding the fundamental physics of earthquake and therefore better preparation for future damaging events. Back-projecting teleseismic high frequency waveforms recorded by a seismic array is an important approach for earthquake rupture imaging. However, the 3D velocity structure effect along the rupture of the earthquake has to be considered to improve the accuracy of such method. Here we propose a new travel time calibration method to calibrate the 3D velocity

structure effect using smaller earthquakes near the mainshock rupture. We validate this method by applying to well-located in-land earthquakes in Japan and then apply it to 2002 Mw7.9 Denali earthquake. Our new result reveals additional details of the earthquake that agrees better with surface rupture trace, finite fault rupture models, aftershocks, and a new prediction from rock mechanics derived from nearby strong motion station PS10. This interdisciplinary application shows its great potential to be generalized to other large earthquake studies.

## 1. Introduction

Detailed constraints on rupture processes of large earthquakes are crucial for understanding fundamental earthquake physics. To image the rupture process of large earthquakes, back-projection (BP) of high frequency (HF) tele-seismic array waveforms is one of the commonly used techniques in the last 15 years or so (e.g., (Ishii *et al.*, 2005, Kruger and Ohrnberger, 2005)). Assuming delta-function shaped Green's functions and taking advantage of the reciprocity between sources and receivers, BP methods trace the location and timing of HF sources by either maximizing the stacking power of back-propagated array data in the time domain (e.g., (Ishii *et al.*, 2005, Yagi *et al.*, 2012)) or the coherence in the frequency domain (e.g., (Meng *et al.*, 2011, Yao *et al.*, 2011, Yin *et al.*, 2016)). The temporal and spatial distribution of HF radiation resolved from BP is usually compared with rupture processes in finite fault models or other observations and models to understand rupture processes of large earthquakes more comprehensively (e.g., (Avouac *et al.*, 2015, Simons *et al.*, 2011)).

BP can image the location and timing of HF sources, hence the rupture speed, as well as the relative strength of the HF sources. The uncertainties of these parameters, if not well-understood, may cause ambiguities and inconsistencies in interpreting BP results and comparing BP results with other results (e.g., finite fault models). In general, sources of uncertainties in BP results can be divided into two categories. The first category is originated from the wavefield complexity, or the violation of the assumption of a delta-function type of Green's function. In a previous study (Zeng *et al.*, 2020), we used deterministic waveform simulations and synthetic tests to analyze the uncertainties caused by waveform complexities from the radiation pattern variation, depth phases and 3D source-side velocity structures. The second category stems from travel-time errors. In general, the travel-time calculated from a certain velocity model (e.g., IASP91 used throughout this paper) is used to back-propagate HF seismic waveforms in BP. However, due to earth's 3D structure, the realistic travel-time may deviate significantly from the model prediction, resulting in potential mislocation of HF sources. The difference between the real and calculated travel-time is thus called travel-time error. To mitigate the impact from the imperfect velocity model in travel-time calculation, a common practice in BP is to align the beginning portion of array waveforms through cross-correlation. In this process, a travel-time correction at the mainshock hypocenter is obtained and then applied to the entire source region, a procedure which is similar to that

used in the master event relocation method. In the latter part of the paper, we call this strategy the “conventional calibration”. However, the source-side 3D velocity structure may be heterogeneous, and corrections derived from the mainshock hypocenter may not be representative in the whole rupture region. Consequently, the conventional calibration may lead to significant mis-location of HF sources in regions far away from the hypocenter.

BP uncertainties caused by the travel-time error have been noticed and investigated by previous studies. For instance, Fan and Shearer (2017) used data recorded by the North American (NA) and global arrays to derive travel-time corrections for events ( $6 < M_w < 7$ ) in eastern Japan subduction zone (JSZ). They then used the travel-time correction from one event to relocate other events and showed that the travel-time error on average could cause  $\sim 25$  km location uncertainty in the BP results, and claimed that such uncertainty is almost randomly distributed. To lessen the influence of the travel-time error, Ishii *et al.* (2007) proposed a weighted interpolation scheme to calibrate the travel-time using aftershocks’ arrival times, and concluded that small scale rupture features were adequately resolved. Palo *et al.* (2014) divided the travel-time error into a ‘static’ term representing the overall travel-time error from the source region and a ‘dynamic’ term accounting for the error between each source-receiver pair and then, based on aftershock arrival times, they corrected the ‘dynamic’ error by interpolating errors in the source region with the kriging method. Meng *et al.* (2016) and Liu *et al.* (2017) showed that the inconsistency between BP results from different arrays might be partially attributed to the travel-time error, and proposed to either calibrate the travel-time from aftershock/foreshock arrivals (Meng *et al.*, 2016) or to calculate the travel-time by using a 3D global velocity model (Liu *et al.*, 2017).

A limitation in using a global 3D velocity model is the low spatial resolution in the rupture scale of most large earthquakes (e.g., featuring 100 – 400 km of rupture length). Furthermore, good 3D velocity models only exist for very few places around the world such as Japan or Southern California. Moreover, regarding aftershock/foreshock travel-time calibrations, there are still some unresolved questions and incompatibilities. For instance, Fan and Shearer (2017) claimed that most of the travel-time errors were due to random 3-D structures around the hypocenter and this prevented further improving BP results using an aftershock/foreshock calibration in the whole east JSZ, while Meng *et al.* (2016) applied a slowness calibration to the 2015 Nepal Mw 7.8 earthquake to derive a higher resolution BP result. Hence, we raise a key question here: is travel-time calibration possible and if so, what is the relevant spatial scale and how one can properly calibrate travel-time errors? Such questions should be addressed based on observations, i.e., directly investigating the travel-time error pattern in the source region, which has not yet been systematically studied.

In addition to the points discussed above, the potential influence from the origin time error (the earthquake depth uncertainty is included here because of the trade-off between the earthquake origin time and depth) of calibration events

has not yet been fully considered in the studies using travel-time calibrations from foreshocks/aftershocks. Actually, the origin time error of earthquakes can be as large as 2 seconds (e.g., the origin time may differ by 1 - 2 s in various catalogs for the same earthquake), which may be comparable to that caused by the 3D velocity structure. This implies that the origin time error of calibration events could have been mapped as the artificial 3D structure effect and thus the calibration may not be effective or even bring extra errors into BP results.

To address these issues, we first take advantage of reciprocity between sources and receivers, and use array (i.e., Hi-Net in Japan) travel-time observations to understand the spatial variation pattern of the travel-time error caused by source-side 3D structure (see the schematic illustration in Figure 1a and b). We also investigate the pattern of the travel-time error caused by the subduction structure using the Hi-Net array records of the earthquakes occurring in the Sumatra subduction zone. These observations are used to clarify whether we can calibrate travel-time errors with linear interpolation and to draw the spatial boundary of applying any calibration. We then, from theoretical point of view, propose a new travel-time calibration strategy that takes into account of the origin time error of calibration events. The new strategy is verified by application to well-located  $M > 5.0$  earthquakes in central Honshu, Japan. In the second half of the paper, we apply the method to derive a path-calibrated BP image for the rupture of the 2002 Mw7.9 Denali earthquake. The new BP result is then interpreted and validated by comparing to the local rupture speed and the super-shear transition location inferred from a near fault strong motion data by using near-fault analytical models (Mello *et al.*, 2016), as well as with surface rupture trace. This is followed by discussion and conclusion of the study.

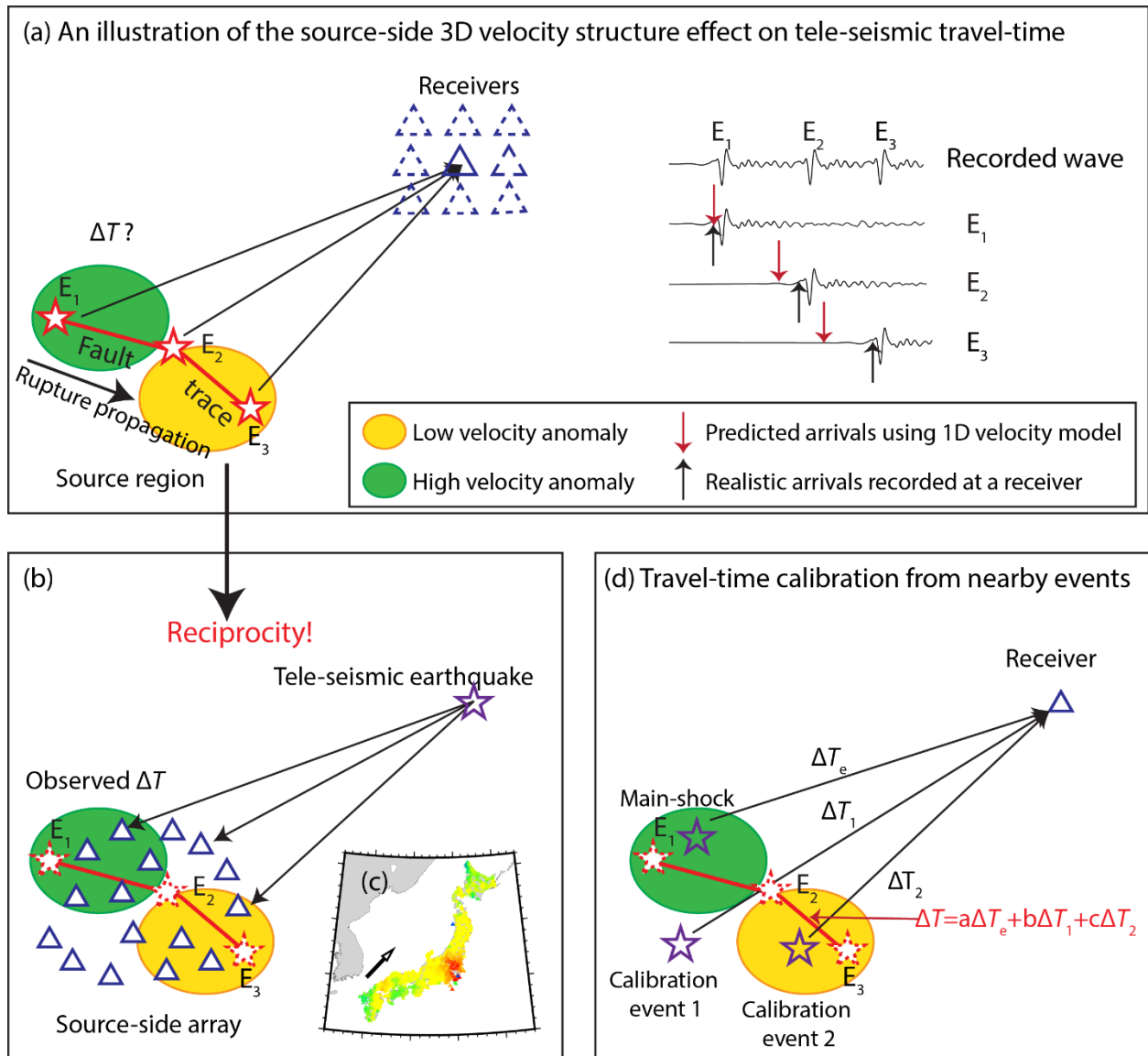


Figure 1 A cartoon illustration of how we investigate the travel-time error ( $\Delta T$ ) in the source region. (a) and (b) show that by taking advantage of the reciprocity, we can use array observations made in the source-side of tele-seismic events to study the travel-time error. An example is shown in (c) (inset of (b)) which will be well explained in section 3. (d) Based on the ray theory (section 2.1) and the observations (section 3 and 4), we propose a linear interpolation strategy to calibrate the travel-time error in the source region.

## 2. Travel-time error observations on the Hi-Net array for tele-seismic

## events

To answer the question whether we can calibrate travel-time error in the rupture area of a large earthquake, we first study how the travel-time error varies with the source locations using direct observations. A natural way to obtain such observations is collecting data in a tele-seismic array for events occurring around the rupture of a large earthquake. However, the number of such events is usually not sufficient, as earthquake magnitude has to be larger than certain threshold (e.g.,  $M > 5.5$ ) to ensure high quality observations. The location and origin time uncertainties of such events also introduce extra difficulties. Luckily, the source-receiver reciprocity, which states that the travel-time from a source to a receiver is identical as that from the receiver to the source, can help resolve this problem. With reciprocity, stations in a dense seismic array are regarded as earthquake sources while a teleseismic earthquake is considered as a station, and therefore the origin time error is a constant and will not contribute to the travel-time error variation observed in the source-side array. Here, we pick Japan as the test ground, as it has extremely dense seismic stations (e.g., the Hi-net array) that have been working for several decades. We download Hi-net array waveforms for 4  $M_w > 6.8$  teleseismic event pairs (Figure S1a) from different back azimuths. For each event, we align the array waveforms by cross-correlation to uniformly pick the P-wave arrivals (see details in 3.2). We then calculate the 1D travel-times and subtract them from the observations to obtain travel-time errors. Here we plot the event pair composed of the 202007220612 and 202010192054 events in Figure 2a-b with other three event pairs shown in Figure S2. Note that, in these travel-time error figures, we already remove the mean value, which could be considered as part of the earthquake origin time error. Throughout the entire area of Japan, at the scale larger than 1000 km, the travel-time error of each event varies as large as 5-6 s and is featured with distributed travel-time error mountains (positive errors) and valleys (negative errors). However, the travel-time errors of these two events are very similar (Figure 2a vs 2b), and their differences are almost zero (Figure 2c). Here we introduce the Mean Absolute Deviation (MAD) ( $MAD = \frac{1}{n} \sum_{i=1}^n |x_i - m(X)|$ , where  $m(X)$  is the mean value) to quantify the dispersion in Figure 2c. Because Figure 2c shows the travel-time error difference (TED) between the two events, we further introduce MADD, which refers to the MAD of the TED. The MADD in Figure 2c is as small as 0.09, suggesting that the travel-time error variation is mainly contributed by the structure beneath the arrays (or source-side structure if we consider an earthquake locates beneath the Hi-net array).

To investigate the travel-time error for a source region of a few hundred km ( $\sim 300$  km), which is the dimension of large earthquakes (e.g.,  $M > 8$ ), we select three sub-regions in Japan (rectangles in Figure 2a), where the travel-time error shows clear variations (Figure 2 d, e, f). To the first order, the travel-time error in all the three regions is systematically increasing/decreasing along certain direction (e.g., in Figure 2d, the travel-time error roughly increases from west to east). We may approximate the systematic variation as a linear trend to the first order and use a ramp function to fit this trend. After removing the best fit ramp functions,

shown as insets in Figure 2d, e and f, the residual travel-time error varies almost randomly (Figure 2 j, k, l) with  $\sim 50\%$  reduction in MADs and all the  $R^2$  values are larger than 0.5. This analysis suggests that the observed travel-time error caused by the 3D structure at the scale of a few hundred km varies dominantly linearly, and using a few calibration earthquakes could effectively calibrate the first order travel-time error using a linear interpolation.

The reciprocity idea works well for land areas, but we don't have a dense seismic array like Hi-net in the ocean. To further understand travel-time errors for a source region in the ocean, we turn off the reciprocity and still use Hi-net array to study a few representative events in the Sumatran subduction zone (Figure 3f), one of the most seismically active regions in the world. We download Hi-net data for five events, pick their P-wave arrival times by cross-correlation, and then calculate travel-time errors relative to the IASP91 1D model. We show travel-time error histograms of these events in Figure 3a-e, which show very similar shape and have almost identical MADs (less than 10% difference). To further evaluate their differences, we use the 200811221601 event located in the most south as the reference event and calculate TEDs between the reference event and other 4 events (similar to Figure 2c), with the TED histograms shown in Figure 3g-j. It appears that when an event is further away from the reference event, the TED histogram has lower peak and is distributed in a broader range (e.g., Figure 3 g vs j), and the corresponding MADD increases. We consider the increase of MADD as a function of distance to the reference event represents a systematic travel-time error variation. We then verify if the MADD vary linearly as the distance to the reference event increases.

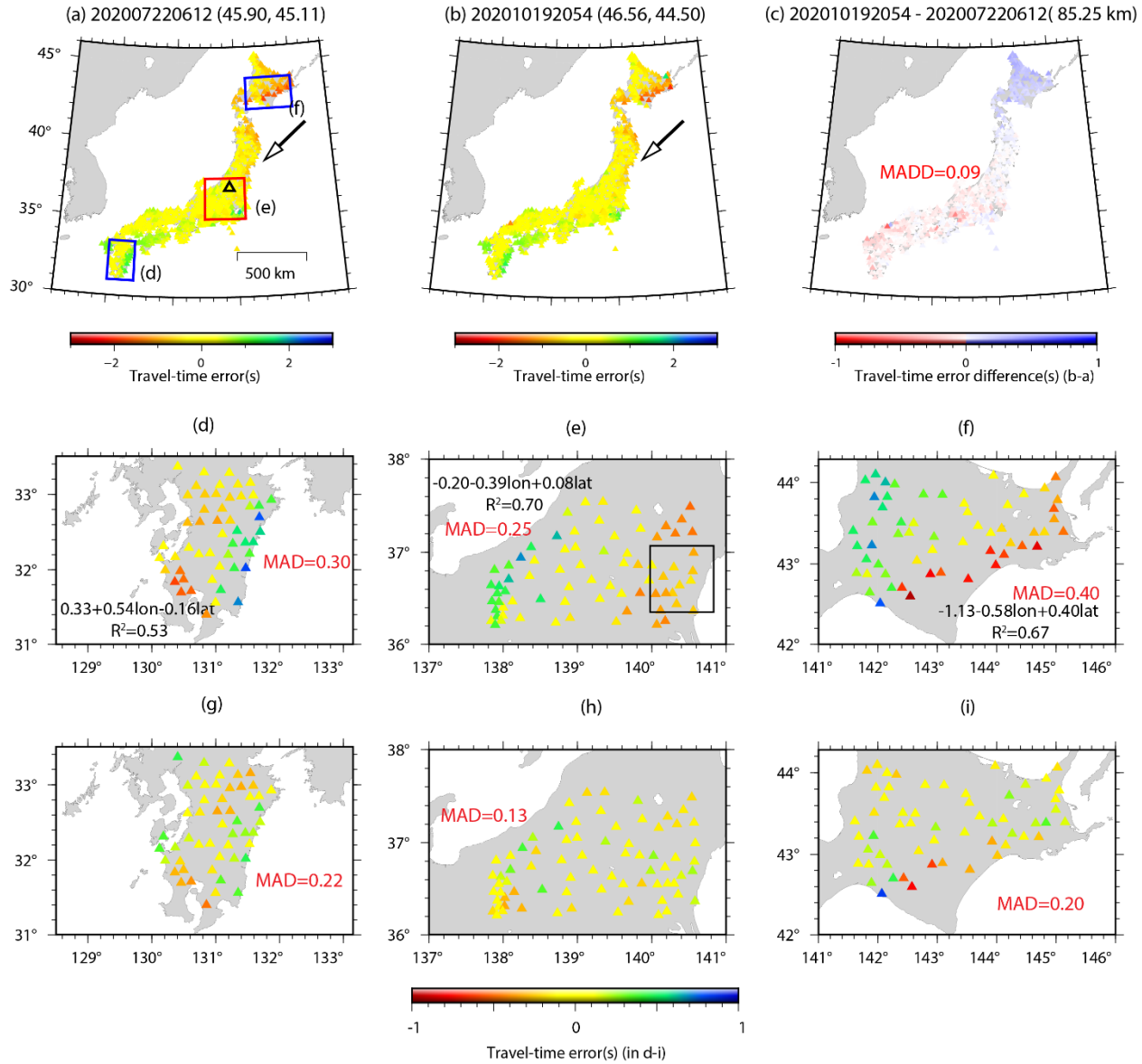


Figure 2 (a-b) The P wave travel-time error between the data and the theoretical 1D (IASP91) calculation for one event pair from northeast. The format of the subfigure titles is event ID (azimuth, great circle distance) and this rule is applied to Figure 6. The azimuth and great circle distance of each event are estimated relative to the station, HMTH (black triangle in (a),  $37.0103^\circ$ ,  $139.376^\circ$ ). The arrows in these subfigures represent the approximate incident P-wave direction. (c) The travel-time error difference between (a) and (b). The distance between each event pair (based on the USGS catalog) is shown in the

bracket in the subfigure title. (d-f) The P wave travel-time error for the event 202007220612 (a) in the three rectangles in (a) which shows dominantly linear variation. The black triangle in (e) exemplifies a region with local complicated variation pattern of the travel-time error. (g-i) The residual travel-time error after removing a plane trend from (d-f). The plane equations and coefficient of determination ( $R^2$ ) are shown in Figure (d-f). Red numbers in (c, d-i) are the mean absolute errors in each subfigure. To account for the elevation difference among stations, we assume a P-wave velocity of 5.8 km/s and subtract a factor of elevation/5.8 from the real arrivals, and this strategy is applied to Figure 6.

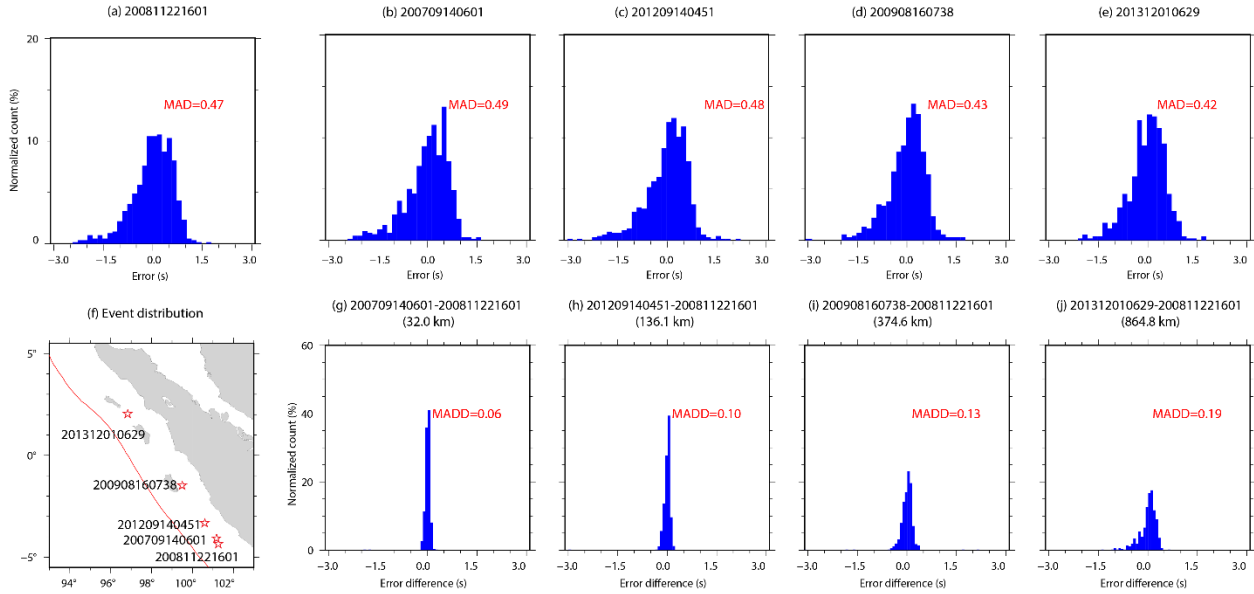


Figure 3. (a-e) Statistic histograms of travel-time errors of 5 representative events (f) along Sumatra subduction zone. (g-j) Statistic histograms of the travel-time error difference with respect to the reference event 200811221601. In the parenthesis in titles of subfigures g-j, we show the distance between an event to the reference event.

To have a more comprehensive assessment, we download Hi-net data for 53 Mw6-7 events that are distributed in a region of  $\sim 1000$  km along the Sumatran subduction zone (Figure 4a). TEDs and MADDs of these events are calculated following the procedure in Figure 3. We present the MADD distribution of all the collected events with respect to two reference events (200811221601 and 200803291730 which are located at the south and north ends of the study region) in Figure 4b-c. With respect to both reference events, to the first order, the MADD increases with the event's distance to the reference event. We further show the relationship between the MADD and the corresponding event's distance to the 200811221601 event. Clearly, the first order feature is a linear variation, consistent with what we observed in Figure 2d-f. Note there are two

outliers (highlighted with blue rectangles in Figure 4b-d) located within shallow crust of the main Sumatran Island and with large MADDs no matter which reference event is selected, suggesting distinct velocity structures of the crust and subduction zone.

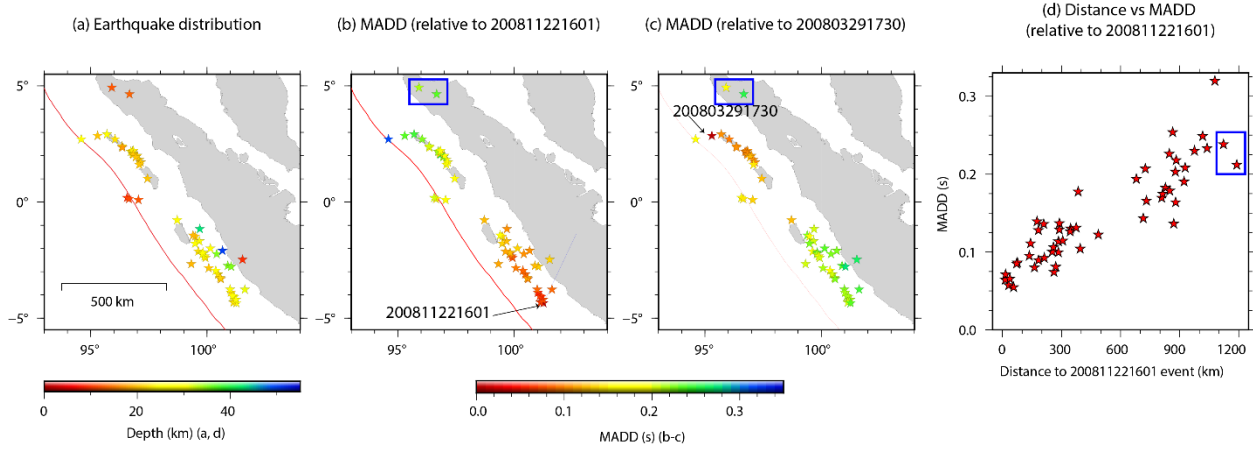


Figure 4. Travel-time error difference analysis for earthquakes in Sumatran subduction zone. (a) Earthquakes used in the study, color-coded by event depth. (b-c) Distribution of MAD of travel-time error difference (MADD) with reference events located in the south (200811221601) and north (200803291730). (d) The relationship between MADD and the distance between events and the reference event (200811221601). Blue rectangles in (b-d) highlights two crustal events which are different than oceanic events in terms of the MADD.

### 3. Travel-time Path Calibration Strategy and Validation

#### 3.1 Travel-time Path Calibration

In previous section, we show that the 3D source-side velocity structure causes the travel-time error to vary dominantly linearly. To construct the linear interpolation using observations, in this section, we first show that the linear variation can also be derived from the ray theory. Then, based on the derived linear variation formula and with simple and specific manipulation, we can reach an interpolation scheme in which the origin time error can be easily isolated.

The theoretical tele-seismic P wave travel-time along a ray path can be written as,

$$T^t = \int_s^r u^t ds \quad (1)$$

where  $u$  refers to the slowness in a reference velocity model,  $s$  is the source location,  $r$  is the receiver location,  $ds$  is the infinitesimal distance along ray path, and superscript  $t$  represents the theoretical calculation. We assume a small slowness perturbation  $\Delta u$  which doesn't change the ray path to the first order (Snieder and Sambridge, 1992), and the perturbed travel-time could be expressed as,

$$T = \int_s^r (u^t + \Delta u) ds = T^t + \int_s^r \frac{\Delta u}{u^t} \cdot u^t ds \quad (2)$$

We rewrite the second term in the right hand side (RHS) of equation (2) as  $\langle \frac{\Delta u}{u^t} \rangle \int_s^r u^t ds = \langle \frac{\Delta u}{u^t} \rangle T^t$ , where  $\langle \frac{\Delta u}{u^t} \rangle$  is equal to  $\frac{\int_s^r \frac{\Delta u}{u^t} \cdot u^t ds}{\int_s^r u^t ds}$  and represents the average relative slowness perturbation along the ray path. Thus, we can express the travel-time error caused by the small slowness perturbation as,

$$\Delta T = T - T^t = \langle \frac{\Delta u}{u^t} \rangle T^t \quad (3)$$

Here, we assume the travel-time perturbation is mostly caused by the source-side 3D structure, as for a tele-seismic station, seismic rays from different parts of a rupture differ most in the source region and converge at the receiver. This is also supported by the travel-time error observations we made (Figure 2&4). We therefore expand the RHS of eqn. (3) to the first order with respect to a reference source location  $e$  (i.e., epicenter of the main-shock),

$$\Delta T = \langle \frac{\Delta u}{u^t} \rangle_e T^t \approx \left( \langle \frac{\Delta u}{u^t} \rangle_e + \frac{\partial \langle \frac{\Delta u}{u^t} \rangle_e}{\partial \mathbf{x}} \cdot \Delta \mathbf{x} \right) T^t = \left( \frac{\Delta T_e}{T_e^t} + \frac{\partial \langle \frac{\Delta u}{u^t} \rangle_e}{\partial \mathbf{x}} \cdot \Delta \mathbf{x} \right) T^t = \left( \Delta T_e + T_e^t \frac{\partial \langle \frac{\Delta u}{u^t} \rangle_e}{\partial \mathbf{x}} \cdot \Delta \mathbf{x} \right) \frac{T^t}{T_e^t} \quad (4)$$

where  $\Delta \mathbf{x}$  is the location vector of an arbitrary point relative to the epicenter and can be expressed as  $\begin{pmatrix} \Delta x \\ \Delta y \end{pmatrix}$  in a two dimensional plane. In the conventional BP procedure, the travel-time correction for the entire source region is assumed to be identical to that from the epicenter (usually achieved by aligning the beginning portion of P-waves) and ignore the contribution of the term  $T_e^t \frac{\partial \langle \frac{\Delta u}{u^t} \rangle_e}{\partial \mathbf{x}} \cdot \Delta \mathbf{x}$  in eqn. (4). We show in section 2 that this second term should be and could be considered. Note that the RHS term is proportional to  $\frac{T^t}{T_e^t}$ , which approximates 1 in most cases as the rupture dimension is usually much smaller than the source-to-receiver distance. For instance, for an array located  $30^\circ$  away from the earthquake (e.g., with a dimension of  $2^\circ \times 2^\circ$ ),  $\frac{T^t}{T_e^t}$  differs from 1 by less than 0.05. However, for earthquakes rupturing ultra-large area, e.g. the 2004 Mw 9.3 great Sumatra earthquake that ruptured more than  $\sim 1400$  km along strike (e.g., Ishii *et al.*, 2005),  $\frac{T^t}{T_e^t}$  can't be assumed to be close to 1. In such a case, one can segment the source region into several pieces to ensure in each piece  $\frac{T^t}{T_e^t} \approx 1$ .

To make correction (i.e., path calibration), we can obtain the second term in the RHS of eqn. (4) using travel-time error of strong aftershocks/foreshocks or historical earthquakes in the rupture area. If we assume there are two more calibration events numbered as 1 and 2 besides the main-shock (for the epicenter), we may estimate the gradient of  $\langle \frac{\Delta u}{u^t} \rangle_e$  as,

$$\mathbf{G}^T = \frac{1}{T_e^t} (\Delta T_1 - \Delta T_e, \Delta T_2 - \Delta T_e) (\mathbf{x}_1 - \mathbf{x}_e, \mathbf{x}_2 - \mathbf{x}_e)^{-1} = \frac{1}{T_e^t} (\Delta T_1 - \Delta T_e, \Delta T_2 - \Delta T_e) \mathbf{C} \quad (5)$$

, where  $\mathbf{C} = (\mathbf{x}_1 - \mathbf{x}_e, \mathbf{x}_2 - \mathbf{x}_e)^{-1}$  is a constant vector,  $(\mathbf{x}_1 - \mathbf{x}_e, \mathbf{x}_2 - \mathbf{x}_e) =$

$\begin{pmatrix} x_1 - x_e & x_2 - x_e \\ y_1 - y_e & y_2 - y_e \end{pmatrix}$ ,  $\mathbf{G}^T = (G_x, G_y)^T = \frac{\partial \langle \frac{\Delta T}{u^t} \rangle_e}{\partial \mathbf{x}}$ ,  $\mathbf{x}_e$ ,  $\mathbf{x}_1$  and  $\mathbf{x}_2$  refer to the epicenters of the mainshock and two additional calibration events, respectively; and  $\Delta T_1$  and  $\Delta T_2$  are travel-time errors from events 1 and 2. Here, we approximate  $T^t$  with  $T_e^t$ . The main advantage of this formula is that it minimizes the influence of the origin time uncertainty of calibration events. To better explore this, we assume three calibration events have origin time errors of  $\delta t_e, \delta t_1, \delta t_2$ , respectively, and we may obtain,

$$\mathbf{G}'^T = \mathbf{G}^T + \frac{1}{T_e^t} (\delta t_1 - \delta t_e, \delta t_2 - \delta t_e) \mathbf{C} \quad (6)$$

For each station, the travel-time correction at an arbitrary location ( $\Delta \mathbf{x}$ ) could be approximated as,

$$\Delta T = \left( \frac{\Delta T_e}{T_e^t} + \mathbf{G}'^T \cdot \Delta \mathbf{x} \right) T_e^t = \Delta T_e + T_e^t \mathbf{G}^T \cdot \Delta \mathbf{x} + (\delta t_1 - \delta t_e, \delta t_2 - \delta t_e) \mathbf{C} \cdot \Delta \mathbf{x} \quad (7)$$

In the RHS of eqn. (7), while the first two terms are station-dependent, because they are functions of either travel-time errors or travel-times, the third term is event-dependent and is a constant for all stations at a given location. As BP uses the differential travel-time between stations to locate HF sources and the third term will be subtracted in this process, the origin time uncertainty may bias the timing of high-frequency radiators, but it barely affects the location.

When there are more than 3 calibrations events, we cluster them into different three-event groups. We then average the travel-time calibration using equation (7),

$$\widehat{\Delta T} = \Delta T_e + T_e^t \widehat{\mathbf{G}_0^T} \cdot d\mathbf{x} + \frac{1}{n} (\sum_{i=0}^n (\delta t_{i_1} - \delta t_{i_0}, \delta t_{i_2} - \delta t_{i_0}) \mathbf{C}_{i_0}) \cdot d\mathbf{x} \quad (8)$$

where  $i$  refers to the  $i^{\text{th}}$  group, and a hat above a variable indicate the average. Alternatively, one can use the least square regression to estimate the average travel-time corrections and the influence from the origin time error can also be isolated, as derived in the supplement material. Based on our experiences, we prefer the 3-event cluster strategy as shown in eqn. (8) rather than the regression, because first, the number of calibration events, which have sufficient high quality waveform records at an array, is usually less than 5, and second, the three-event strategy is more flexible in choosing events to achieve a better spatial coverage of the source region. We do not consider other more sophisticated regressions, because they may cause the coupling (i.e., multiplication) between the origin time error and the travel-time error/the travel-time, leading to the station-dependent influence of the origin time error and causing trade-offs between location and timing of HF radiators. Carefully adjusting optimization parameters in a complicated regression may be helpful, but the computational cost increases rapidly and additional uncertainties may be introduced. A scenario showing the advantage of the 3-event cluster strategy is shown in Figure S3.

### 3.2 Data processing for BP

In order to test the performance of this new calibration strategy, we first perform a validation test and then we apply our new methodology to the 2002 Mw 7.9 Denali earthquake. In this section, we describe the general data processing procedure that is common in these applications. For the earthquakes used in this study, we download their seismic waveform data from IRIS through the SOD (Standing Order for Data) software and from NIED using HinetPy (10.5281/zenodo.4599566). We then check the data quality and align the waveforms for each event by the following process. For  $M > 6.0$  events, we first filter their waveforms into 0.2 - 1.0 Hz, and align the first 6 - 10 s of the waveforms by using the Python package AIMBAT (Lou *et al.*, 2013). We then keep the data with SNRs (generally  $> 3.0$ ) and high cross-correlation coefficients (CCs, generally  $> 0.8$ ) with the stacked waveform template. For  $M < 6.0$  earthquakes, we first select the frequency range (e.g., 0.2 - 1.0, 0.3 - 1.0 or 0.4 - 1.0 or 0.5 - 1.0 Hz) that produces the largest number of traces with clear eye-determined P-wave arrivals and we align the first 5s of waveforms by using AIMBAT. We then look into the waveforms to identify the cycle skips. For the waveforms that have the cycle skip, we manually pick their P-arrival, limit the time shift to less than 2s, cross-correlate every waveform with the stacked array template, and re-align them based on the CCs. Finally, we remove those traces whose first 3 - 5 s are not in an eye-determined coherence with most of the other traces. As only travel-time of calibration events are used, we filter different calibration events at slightly different frequency bands to obtain more coherent and high-quality waveforms. After aligning the waveforms, we calculate the difference of the travel-time errors between different calibration events (i.e., double difference), and drop the stations with exceptionally large absolute values (generally, larger than 3 MADs). These large travel-time error differences may be caused by the instrument issue (e.g., errors in GPS timing), or very local velocity structures (e.g., micro-basins). The processed data are then back-projected to the source region to trace the HF radiation using the MULTIPLE Signal Classification (MUSIC) method (Meng *et al.*, 2011, Zeng *et al.*, 2020).

### 3.3 Validation of the New Travel-time Calibration Strategy

A natural way to validate the new BP calibration strategy is to relocate medium size earthquakes (can be considered as point sources) with and without the calibration and compare the relocations with a high quality catalog, similar to that in Fan and Shearer (2017) and Meng *et al.* (2016). Here we select the inland earthquakes occurred in Kanto and Chubu regions of Japan (the red rectangle in Figure 2a) where observed travel-time errors from a tele-seismic event are characterized with near linear variation (e.g., Figure 2e, h). There are near 50 shallow events with magnitude (USGS) greater than 5.0 in the last 20 years, and they were well recorded by the dense local array, which was used to derive the high quality JMA catalog, and the dense North American (NA) array (Figure S1c), which will be used to validate our calibration strategy. To establish path calibration, we select 3 calibration events that have good coverage of the region. The selected earthquakes are represented by red (201411221308 Mw 6.2) and blue (200707160113 Mw 6.6 and 201104110816 Mw 6.6) stars in Figure

5a. We use travel-time errors of these events to calibrate the path towards NA with the proposed interpolation strategy. We then apply the calibration to relocate other events through BP (Figure 5c) and compare the results to those derived from the conventional method which only uses the 201411221308 earthquake as calibration event (Figure 5b), the latter mimicing the calibration from the mainshock epicenter. As expected, single event calibration works well for earthquakes close to the calibration event (Figure 5b). But the mismatch between the BP results and the JMA epicenters increases gradually as the events' distance to the calibration event increases (Figure 5d), primarily because the 3D structure effect away from the calibration event cannot be effectively corrected. The single-event calibration result is systematically biased toward west relative to the JMA catalog (Figure 5b), indicating a systematic effect of source-side 3D velocity structure. With the 3-event path calibration, the BP location agrees systematically better than that derived from single event calibration (Figure 5d), and there is no obvious systematic location mismatch in the 3-event calibration results (Figure 5c). Near the east coast (the rectangle area in Figure 5a), the BP location shows larger discrepancy relative to JMA location, which is still better than the single-event calibration result ( $11.2 \pm 5.7$  km vs  $16.6 \pm 4.3$  km). This discrepancy could be due to very localized (e.g., the rectangle area in Figure 2e) travel-time error that varies differently than the overall pattern in the study region. Here we consider the discrepancy between the catalog location and BP location as the lower bound estimation of the BP uncertainty, which is also applied to the Denali earthquake case study.

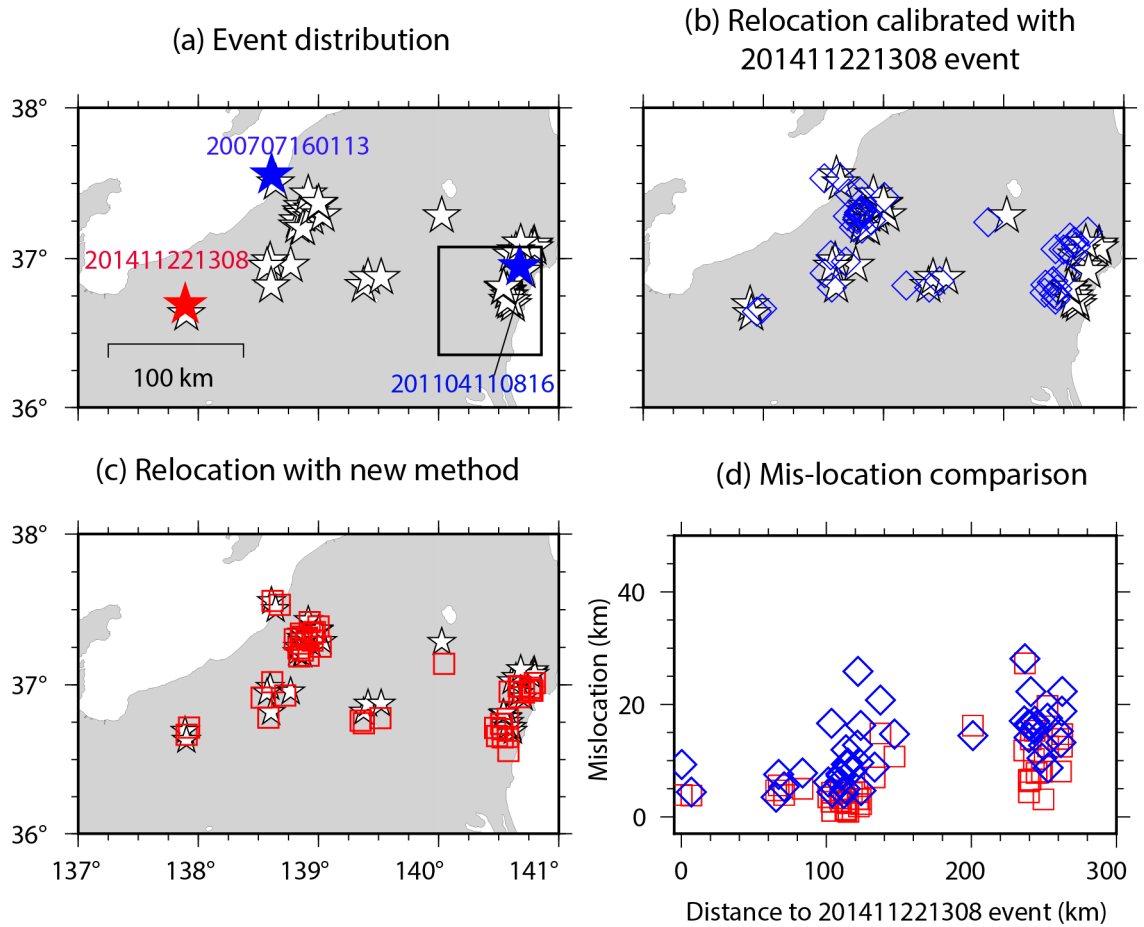


Figure 5. Comparison between conventional BP (i.e., using one single calibration event) with our proposed strategy. (a) Earthquakes with magnitude  $> 5.0$  (USGS) occurred in this region in last 20 years. The red star shows the event used in conventional BP calibration to relocate earthquakes, and red and blue stars are events used in our proposed method to relocate earthquakes. (b-c) Relocation with calibration using one event (red star in (a)) (b) and three events (red and blue stars in (a)) (c). (d) The relationship between the mis-location in either method and the true event distance (calculated using JMA location) to the 201411221308 event. The black rectangle in lower right of (a) is the same as that in Figure 2e and highlights events still showing relatively larger mis-location with our new method.

#### 4. Application to the 2002 Mw7.9 Denali, Alaska Earthquake

To further evaluate the performance of the new path calibration algorithm, we apply our method to a representative large event, the 2002 Mw 7.9 Denali earthquake. We select this event based on the following technical reasons. First,

in the source region of the Denali earthquake, there are tens of local seismic stations, which have been recording many tele-seismic events from various azimuths, providing sufficient travel-time observations to verify that the source-side 3D velocity structure affects the travel-time error linearly. Second, the Denali earthquake ruptured mostly the shallow portion of the crust and therefore the impact of depth phases to the BP results is relatively small (e.g. (Zeng *et al.*, 2020)). Third, the well-mapped surface rupture can be used to verify the BP result. Fourth, the existence of good quality data from the near-fault, PS10 strong motion station ( $\sim 3$ km away from the fault and  $\sim 85$  km to the east of epicenter), allows us to validate our results through comparison to methods based on dynamic rupture mechanics (Mello *et al.*, 2014, Mello *et al.*, 2016).

The earthquake started as a thrust rupture on the Susitna Glacier Fault (SGF), which triggered the unilateral strike-slip rupture on the Denali Fault (DF) that produced a 218-km long surface offset trace. Then the rupture branched onto the Totschunda Fault (TF) and propagated at least 76 km before it stopped (Eberhart-Phillips *et al.*, 2003). Overall, the earthquake ruptured  $\sim 340$  km along strike and lasted for  $\sim 100$  s. The earthquake has been identified as a super-shear rupture event. The ability of dynamic, interfacial, shear ruptures to transition from sub-Rayleigh to super-shear rupture speeds and to propagate at these speeds for very long distances was first experimentally demonstrated in early “laboratory Earthquake” experiments featuring both coherent and frictional interfaces (Rosakis *et al.*, 1999, Rosakis, 2002, Xia *et al.*, 2004). The resulting ultra-fast ruptures are called “super-shear” or “inter-sonic”. This physical rupture mechanics phenomenon which has been known to happen at various scales and has been observed in both engineering and geophysical systems (Rosakis, 2002, Rosakis *et al.*, 2007, Rosakis *et al.*, 2020) is of relevance to the present discussion. Regarding the Denali earthquake rupture of interest here, Dunham and Archuleta (2004) studied this transition numerically and identified a super-shear rupture pulse and a trailing Rayleigh pulse generated following the super-shear transition, and reproduced the rupture pulses through dynamic rupture simulations. Such super-shear-induced double-pulses features are clear signatures of a speed transition event and were also observed in scaled experiments (e.g., Mello *et al.*, 2014) designed to reproduce scaled versions of the Denali earthquake, its transition distance and the PS10 record, in the laboratory. However, despite the fact that there is general agreement that a sub-Rayleigh to super-shear rupture speed transition occurred during the Denali event once local strong motion data especially the PS10 records were analyzed (e.g., Aagaard and Heaton, 2004, Dunham and Archuleta, 2004, Ellsworth *et al.*, 2004), different studies show discrepancies in their prediction of its exact location and timing.

For example, Asano *et al.* (2005) inverted strong motion and GPS data and showed the super-shear rupture segment might be located between 70-80 km and 120-145 km east from the epicenter, while Frankel (2004) inverted local to regional (3-300 km from the earthquake) seismic data and found that the velocity of the rupture 130-220 km east of the epicenter was  $\sim 5.0$  km/s (super-shear speed). Oglesby *et al.* (2004) used local seismic (without PS10) and GPS

data and resolved a rupture speed of 3.3 km/s. Meanwhile, they also claimed the easiest way to better fit PS10 records was to employ a super-shear speed of the rupture. Indeed, most efforts to better explain the particle velocity recorded by PS10 suggested that the Denali rupture propagated at super-shear speed at least when it passed the PS10 station (Dunham and Archuleta, 2004, Ellsworth *et al.*, 2004, Mello *et al.*, 2014). Possibly due to limited resolution, co-seismic slip models inverted only using teleseismic data show the rupture had relatively high average velocity ( $\sim 3.0$  km/s, e.g., (Ji *et al.*, 2004, Ozacar and Beck, 2004, Liao and Huang, 2008)) but not super-shear speed. BP results from teleseismic data differed from most of the results, though super-shear speed was suggested. For example, Walker and Shearer (2009) back-projected tele-seismic European and NA array data and suggested that the super-shear rupture started  $\sim 100$  km to the east of the epicenter, and persisted for at least 200 km with up to 5.8 km/s rupture speed. On the other hand, back-projection of the Hi-Net array data showed the earthquake transitioned to super-shear speed near the epicenter (Wang *et al.*, 2016). And so far, the rupture history details (e.g., rupture speed and transition location to super-shear rupture) from analyzing the PS10 records have not yet been compared with the predictions of BP.

To better understand the rupture process of the Denali earthquake and provide further insights into the discrepancies in the published results, we conduct BP analysis with the proposed new calibration strategy. Together with the new BP results, we employ a multi-disciplinary and multi-scale validation approach whose aim is to reconcile predictions from seismology, dynamic fracture mechanics and field observations.

Here, we first investigate the travel-time error caused by the source-side 3D velocity structure using the local seismic array deployed around the Denali region. We then select two aftershocks further away from the mainshock epicenter to calibrate the paths towards the NA array. These calibrations are applied in the BP analysis to derive a new rupture image of the mainshock, which is compared with rupture parameters derived from other studies, including that from the PS10 strong motion observation and surface rupture mapping. This is followed by a discussion and conclusion of this case study.

To understand the source-side 3D velocity structure effect, we download data on the local array for four tele-seismic earthquakes ( $M > 5.8$ , Figure S1b) from back azimuths consistent with the NA array direction and present their P-wave travel-times relative to the IASP91 model in Figure 6. These travel-time errors could be as large as 3 s, suggesting a path calibration is needed. From visual inspections, these travel-time errors vary mostly linearly. After removing a ramp function, the MADD value drops by 30% to 50%, supporting the linear interpolation for travel-time path calibrations.

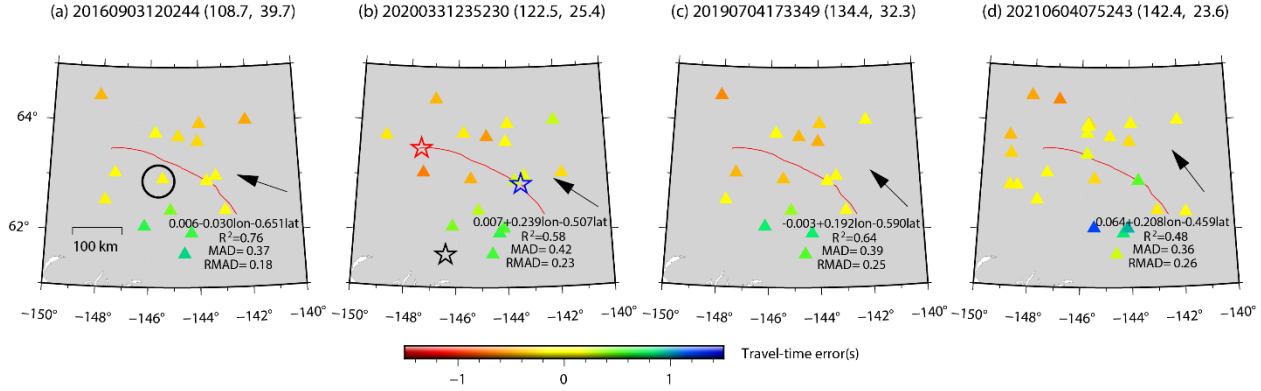


Figure 6. The travel-time differences between the observed P arrivals and the theoretical 1D calculation in the Denali region using tele-seismic events with event timing, back azimuth and epicenter distance shown on top of each panel. The azimuth and great circle distance of each event are estimated relative to the station PAX (black circle in (a)). The arrows represent the incident P-wave direction, and the red lines indicate the rupture trace of the Denali main-shock. For each event, we fit the travel-time errors with a planar equation, which is shown with the coefficient of determination ( $R^2$ ), along with the MAD and RMAD (residual MAD). The red, blue and black stars in (b) refer to Denali main-shock, 200211082029 and 200408250222 events, that are used for the path calibration.

To make interpolation for travel-time corrections as proposed in section 3, we use the main-shock (i.e., epicenter) and two other calibration events (see Figure S4 for their waveforms) that have clearest records in the NA array (Figure S1d) and a good coverage to the rupture area (Figure 6b). Note that we select an event that is  $\sim 300$ km away from the surface rupture to the south (black star in Figure 6b), this turns out to be necessary as it provides the sampling of strong travel-time gradient in this area. We then validate the calibration by relocating  $M > 5$  events along the rupture of the mainshock (Figure 7b) and comparing with conventional calibration results (Figure 7a) and catalog location (white stars in Figure 7a, b). Similar to the previous validation test, the conventional calibration works well near the main-shock epicenter, but as distance increases away from the epicenter, the relocation deviates increasingly from the catalog location towards east. The average mismatch is 49 km for all the events, with peak value  $> 60$  km. In comparison, the new calibration relocates events well and no systematic location deviation. The relocations on average are  $13 \pm 8$  km away from the catalog location. Therefore, we use 13 km as the lower bound estimate of the BP location uncertainty and use it in the following analysis. We also apply similar calibration to the EU array, with waveforms and results shown in Figure S5, but because EU array did not record sufficient high-quality data for the two smaller calibration events, we mainly focus on analyzing and interpreting the result from the NA array.

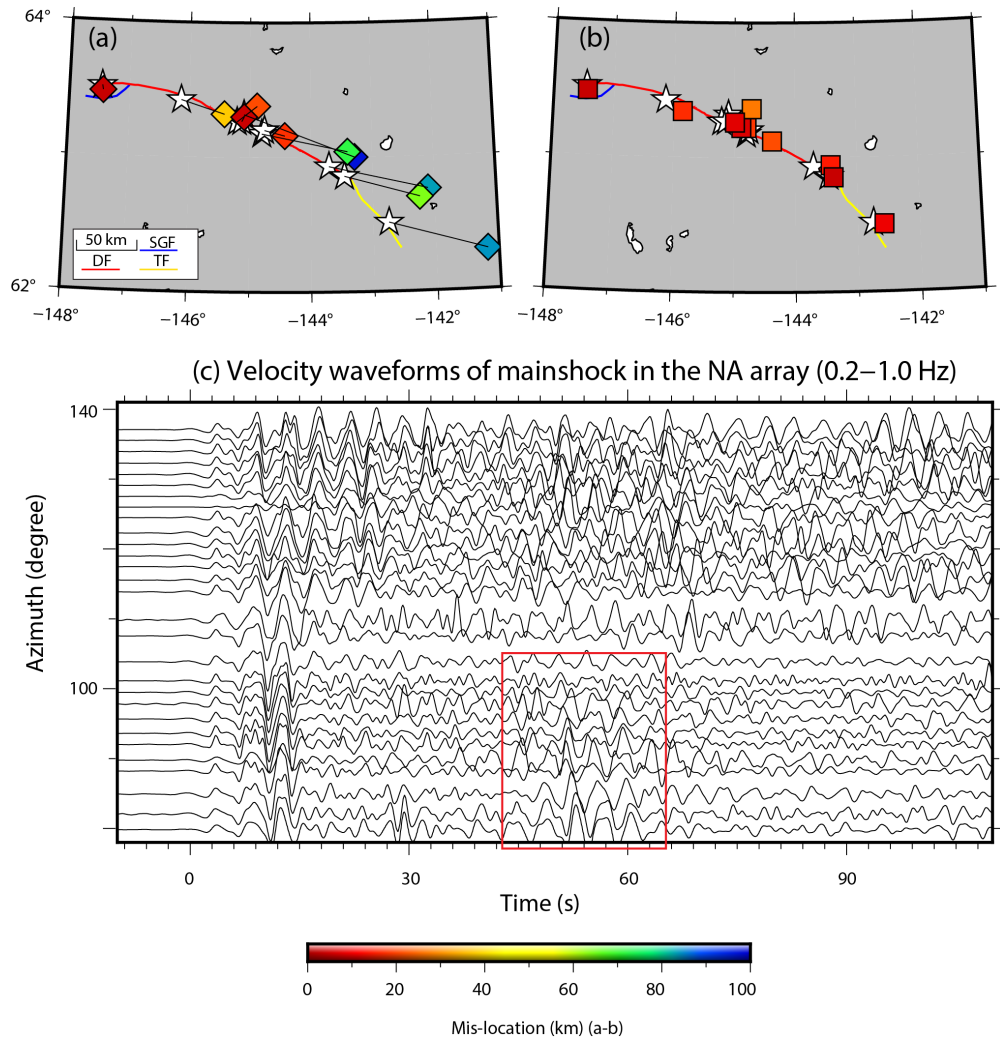


Figure 7. Relocation of near fault earthquakes ( $M > 5$ ) using conventional calibration from mains-shock initial rupture (epicenter) (a) and using new calibration (b). White stars indicate USGS catalog locations and diamonds and squares are BP relocations colored by mis-location relative to the catalog location. Black lines in (a) connect BP locations and catalog locations for each pair. (c) Velocity waveforms of the main-shock in the NA array. The red rectangle highlights the waveform train corresponding to the rupture stagnation in BP result (Figure 8d).

The path-calibrated BP result for the Denali earthquake is shown in Figure 8a, c and d. The locations of HF radiators agree well with the surface rupture trace, mostly located less than 15 km away. This value is also consistent with the 13-km location uncertainty estimated earlier. The BP result reveals a clear

three-stage rupture of the earthquake (Figure 8d). The first stage rupture propagated eastwards from the epicenter for  $\sim 25$ s at a relatively low, sub-Rayleigh speed of  $\sim 1.4$  km/s on the SGF that was reported as a thrust fault (Eberhart-Phillips *et al.*, 2003). Then the rupture propagated onto the DF, accelerated to a super-shear speed of 5.6 km/s (a speed close to the pressure wave speed) and propagated at this speed for  $\sim 20$  s. Between the first and second stage, there is a  $\sim 30$ -km gap with little high frequency radiation, and we interpolate the high frequency radiators to estimate the rupture speed of  $\sim 2.8$  km/s, which approximates the Rayleigh wave speed. The third stage of the rupture was hosted on the last segment ( $\sim 60$  km) of the DF and almost the entire TF. The rupture speed of the third stage ( $\sim 5.2$  km/s) was smaller than the second stage but still super-shear. Although the rupture speed of the later rupture is usually subject to larger uncertainty due to the coda waves from previous rupture, the excellent agreement between the third stage rupture with the surface rupture still results in high confidence. Between the second and the third stages, the rupture decelerated or stagnated for  $\sim 15$ s, and the corresponding signals could be clearly seen in the wave train as highlighted in Figure 7c. The stagnated/decelerated rupture may have dissipated additional strain energy and therefore resulted in a slightly lower rupture speed compared with the second stage. The rupture finally decelerated at the end of TF. The relative weak HF power radiated from DF and TF compared with that from SGF is consistent with the high-frequency energy release per unit fault length analysis from strong ground motion data (Frankel, 2004). The high frequency energy contrast between the early and later ruptures can also be observed in waveform record (Figure 7c). As predicted by the theoretical rupture-dynamics analysis and the lab experiments (Mello *et al.*, 2016), the super-shear rupture speed at a specific location on the fault can be inferred by the ratio of maximum amplitude of the particle velocity between the fault parallel (FP) and fault normal (FN) components (Figure 9). To our knowledge, this technique which is based on the asymptotic structure of a dynamically growing super-shear rupture, has never been used to directly estimate rupture speed for any earthquake perhaps because of the sparsity of near fault records available. Even more surprisingly, this remains true even for the Denali earthquake, despite the fact that the near-fault PS10 FN and FP records have been available for almost two decades. Based on the PS10 records, the FP and FN velocities ratio is found to correspond to a rupture speed of  $1.71C_s$  (Figure 9), which is  $\sim 5.6$  km/s assuming a local shear wave velocity of 3.3 km/s (Brocher *et al.*, 2004) This estimation is very consistent with that derived from the current BP result, which also predicts a rupture speed of  $\sim 5.6$  km/s. Note that the separation time between the super-shear and trailing Rayleigh pulses on the PS10 record is  $\sim 2.6$ s. Assuming a speed of 5.6 km/s for the super-shear rupture and a speed of 3.0 for the trailing Rayleigh pulse, we further derive that the super-shear rupture initiated  $\sim 19$  km to the west of the PS10 station (the red star in Figure 8a and c), using the rupture mechanics method in Mello *et al.* (2014). Following this argument, we now attribute the 30-km gap between stages one and two, as the transition from sub-Rayleigh to super-shear rupture. This super-shear transition location is highly consistent with that estimated from the

BP result (Figure 8d). The transition length ( $\sim 30$  km) is also consistent with scaling lab experiment results to real earthquake (Mello *et al.*, 2014, Xia *et al.*, 2004).

Another interesting feature of our results is that the rupture stagnated on the DF at  $\sim 160$  km to the east of the epicenter for a period of  $\sim 15$  s. It then continued at a super-shear speed and did not slow down when it branched onto the TF branch. It appears that the rupture stagnation is located at the beginning part of the largest asperity, as indicated by surface offsets (Figure 8c) and by the moment release distribution on the fault (Figure 10). Such stagnation could be explained as the slowing down of the rupture when encountering a barrier. Eventually, the barrier was broken and the rupture reaccelerated to super-shear. The process could be facilitated by concentrated stress near the barrier either from the focusing effect of the rupture front (e.g., Dunham *et al.*, 2003) or from the stopping phases generated by the rupture slowing/stopping near the barrier (e.g., Weng *et al.*, 2015). This type of super-shear is thus called the barrier-induced super-shear. There are several possible reasons that the super-shear rupture did not continue on the DF but branched onto the TF without slowing down. Based on paleo-seismological investigations, the accumulated slip deficit on the TF (2.77m – 5.29m) is much larger than that on the DF branch (0.62 – 3.65 m) (Schwartz *et al.*, 2012), suggesting that the TF might be closer to failure. Indeed, Klinger *et al.* (2017) found that long-term geomorphology indicates the existence of a strong asperity in the zone where the rupture branched off the main fault. The effect of dynamic rupture propagation additionally favored rupture branching into the dilatational quadrant of the main fault rupture where TF is located (Kame *et al.*, 2003, Bhat *et al.*, 2004). Another explanation is also possible. As it is shown in both numerical simulations (Kame *et al.*, 2003) and lab experiments augmented by theory (Rousseau and Rosakis, 2003), the larger the rupture speed, the easier the rupture will continue along a branched fault line. This is consistent with our current BP results which suggest the rupture propagated at super-shear rupture speed in the third stage and furthermore the rupture did not slow down when branching from DF onto TF. Indeed, lab experiments (Rousseau and Rosakis, 2003, Templeton *et al.*, 2009) clearly show that ruptures did not slow down dramatically when and after encountering a branch on a fault if the incoming rupture speed was super-shear and the branching angle was  $\sim 30^\circ$  (approximately the angle between DF and TF (Schwartz *et al.*, 2012)) in the dilatational quadrant of the main fault rupture (see Figure 16 in Rousseau and Rosakis (2003)). The above discussed observations are all in line with the super-shear rupture speed histories that we observed, based on the present BP methodology, before and after the rupture branched onto the TF.

Comparisons between HF radiators in BP result and surface offset observations (Haeussler *et al.*, 2004) (Figure 8c) and slip models (Figure 10) (Hreinsdóttir *et al.*, 2006, Oglesby *et al.*, 2004) show that most of the HF radiators are located between slip patches. Although the slip models were derived from different datasets and inversion methods, their first order features, e.g., distribution of large slip patches on DF, are quite similar. The HF radiators almost co-locate

with the aftershock clusters (Figures 8, 10), which suggests that the co-seismic rupture did not fully release the stress on these portions of the faults. The incomplete rupture areas on the faults could be associated with shorter rise time and changes of rupture speed that also enhances the radiation of high frequency energy.

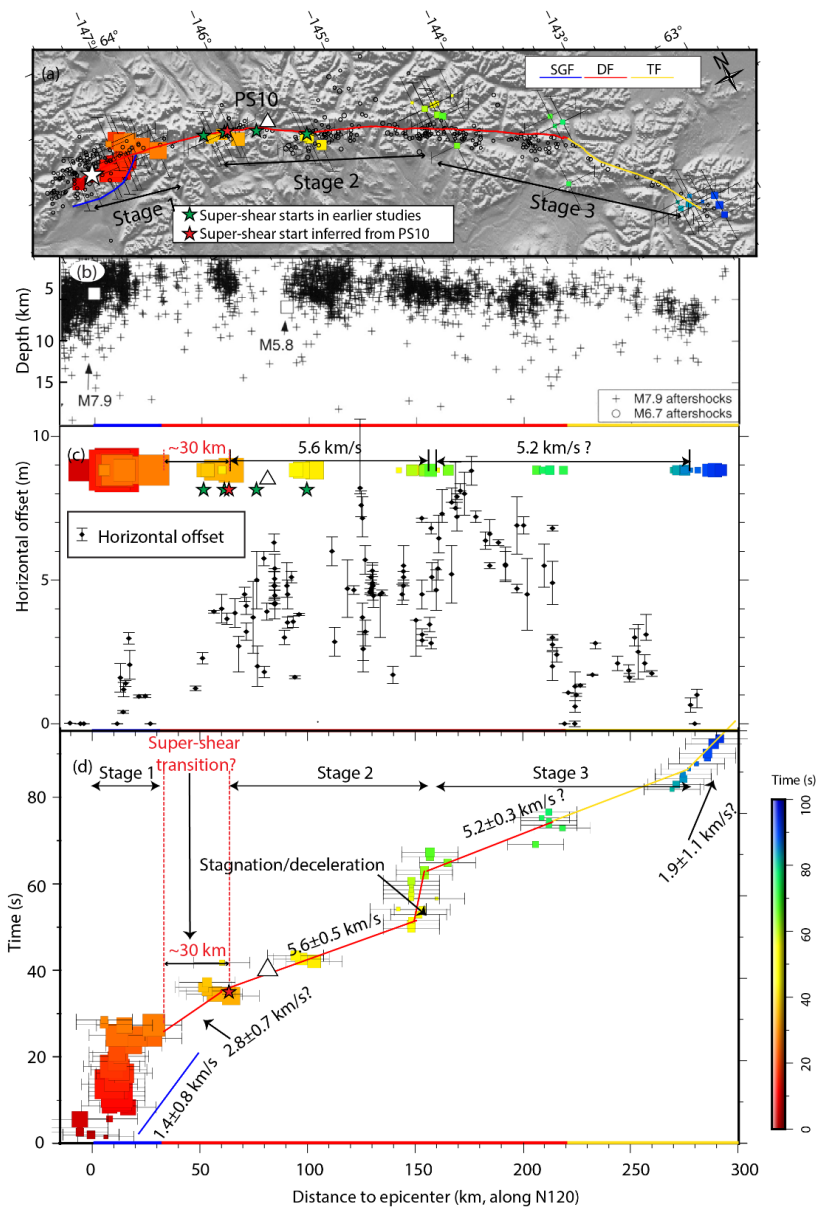


Figure 8 (a) NA array BP result after path calibration. Circles are aftershocks (USGS catalog) with magnitude  $> 3.5$  in the first month following the mainshock. The white triangle (same as in b-d) shows the location of the strong motion station PS10. The squares are sized by their beamforming amplitude and colored by their timing. (b) Depth distribution of aftershocks in  $\sim 1.5$  months after the main-shock (modified from Figure 7 in Ratchkovski *et al.* (2003)). (c) Comparison of BP result with horizontal offsets from (Baize *et al.*, 2020, Haeussler *et al.*, 2004). (d) Time and the distance of HF radiators relative to the USGS epicenter and origin time, and the corresponding rupture speed estimations, as indicated by the lines and numbers. Green stars in (a) and (c) are estimated starting location of super-shear rupture in the literature, from left to right are Dunham and Archuleta (2004), Ellsworth *et al.* (2004) (also Mello *et al.* (2014)), Asano *et al.* (2005) and Walker and Shearer (2009). Red star in (a) (also in panel (c)) is the inferred start of super-shear from analyzing PS10 records (Figure 9), which is overlapping with that from (Dunham and Archuleta, 2004, Mello *et al.*, 2014). SGF: The Susitna Glacier thrust Fault. DF: The Denali Fault. TF: The Totschunda Fault.

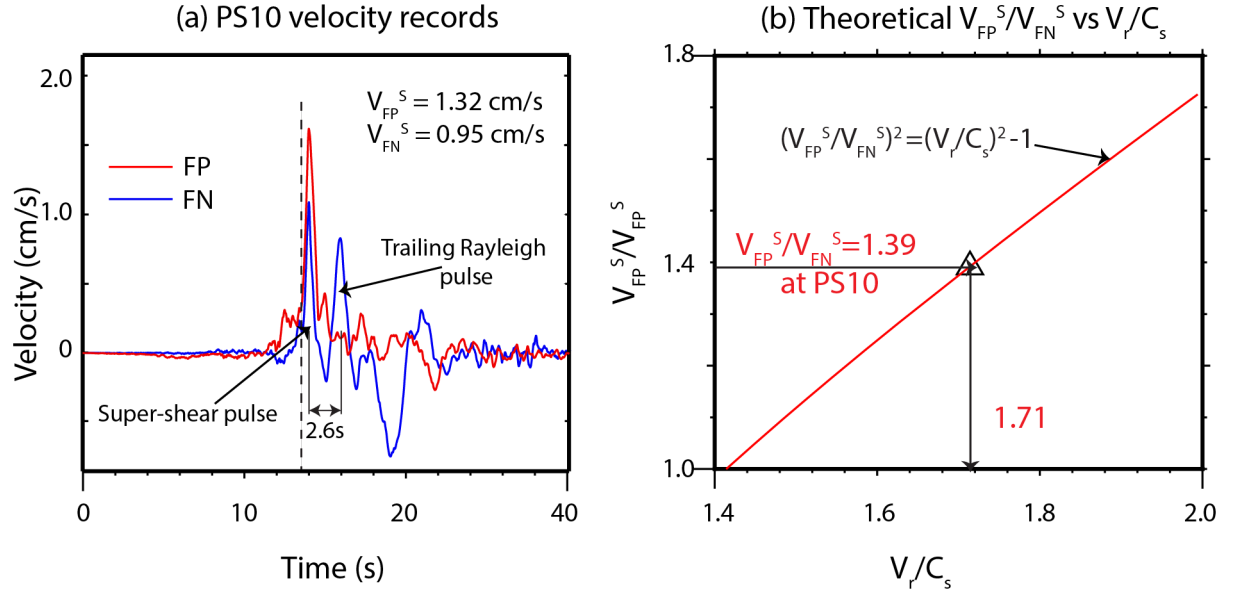


Figure 9. (a) The recorded fault parallel (FP) and fault normal (FN) velocity waveforms at the PS10 strong motion station (Ellsworth *et al.*, 2004). The dash vertical line marks the arrival of the shear Mach front.  $V_{FP}^S$  and  $V_{FN}^S$  are FP and FN velocity jumps induced by the shear Mach front, which are measured as the peak velocities relative to the velocities at the shear Mach front arrival (the dashed line). The 2.6 s indicates the separation between the super-shear and the trailing Rayleigh pulses. (b) Theoretical relationship between the maximum FP an FN particle velocity amplitudes  $V_{FP}^S/V_{FN}^S$  and  $V_r/C_s$  based on Mello et

al. (2016). The amplitude ratio measured from PS10 station is indicated by the triangle, which is corresponding to a rupture speed ( $V_r$ ) of  $1.71C_s$ , here  $C_s$  is the shear wave speed.

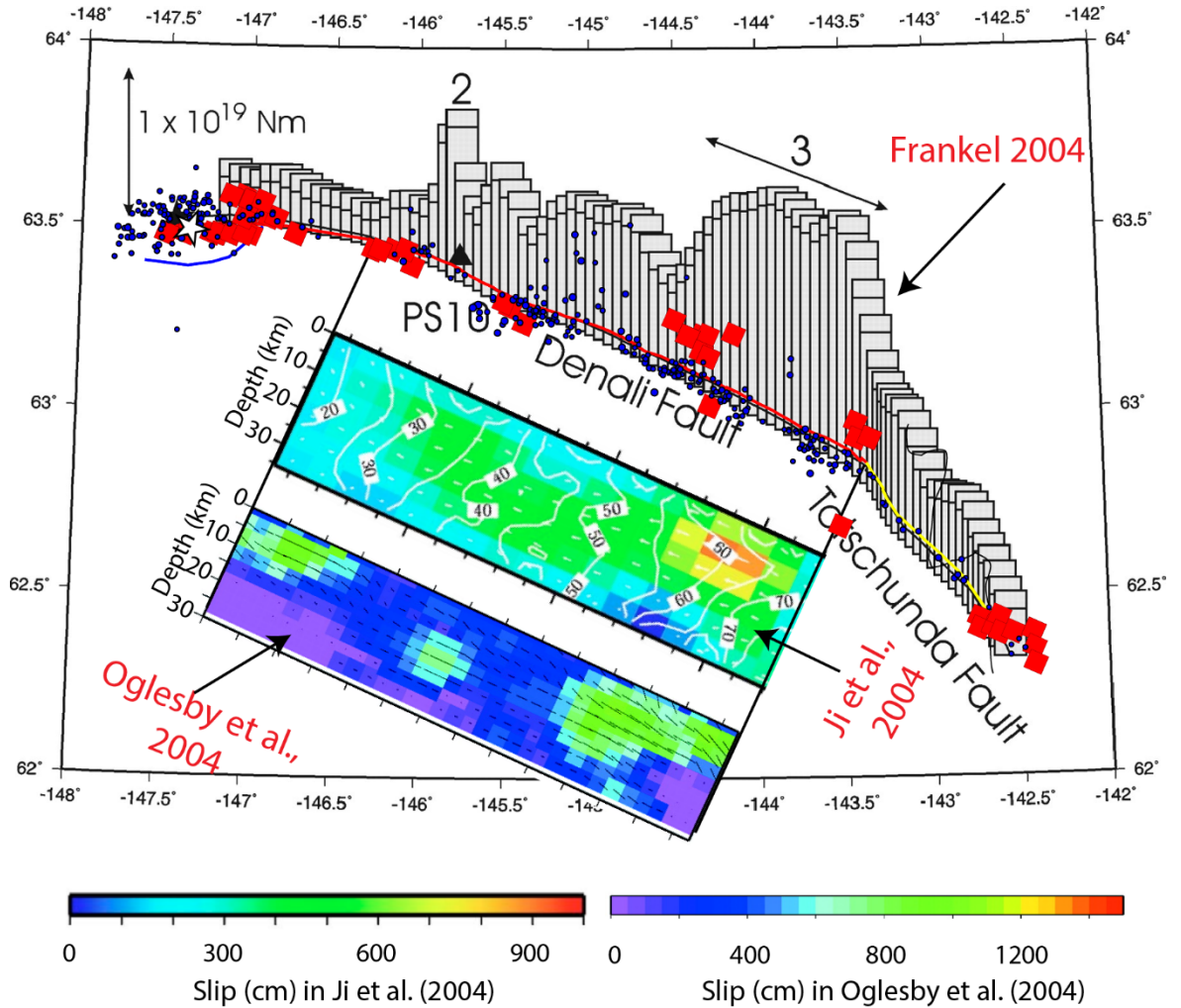


Figure 10. Comparison between BP results and various co-seismic slip models. We overlap the BP result (red tilted squares) with Figure 4 in Frankel (2004). The blue dots are  $M > 3.5$  aftershocks. The columns represent strike slip moment release along the strike in Frankel (2004). We also show two slip models (Ji *et al.*, 2004, Oglesby *et al.*, 2004) for the central Denali fault segment.

## 5. Discussion and Conclusion

### 5.1 The BP method

The idea of using the reciprocity and MADD to investigate travel-time errors

can be generalized to other regions, in particular for subduction zones, which are known for their extreme seismic activity and structure complexity. The array observations can improve our understanding of the impact of 3D structure at various wavelengths from tens of kilometers (e.g., micro-basins) to a few hundred kilometers (e.g., subducting slab). One of the key features in such array observations is the azimuthal dependency of the patterns of the travel-time errors. For example, Figure 11 shows the travel-time error around Kantō plain in Japan for earthquakes coming from four different back azimuth (indicated by the vectors), where clear differences can be observed. The most dramatic difference is between the first (202007220612) and the third (201908021203) panels. For the earthquake located to the southwest (third panel), the Kantō plain shows large travel-time delay relative to the 1D prediction while the same region shows travel-time advancing for an earthquake located to the northeast (first panel). This is likely a result between the competition of the basin structure (slow) in Kantō plain and the subducting slab structure (fast). The northeast event ray paths could have sampled a large portion of the subducting Pacific slab for stations in the basin, and therefore cancel out and partially outcompete (blue triangles) the basin effect. The southwestern event ray paths may mostly sample the basin structure and show the most dramatic travel-time delays. The other two events may sample the structure between these two extreme cases. Future detailed study could be conducted to better understand the gradual variation of the array travel error distribution and their impact in the back-projection studies.

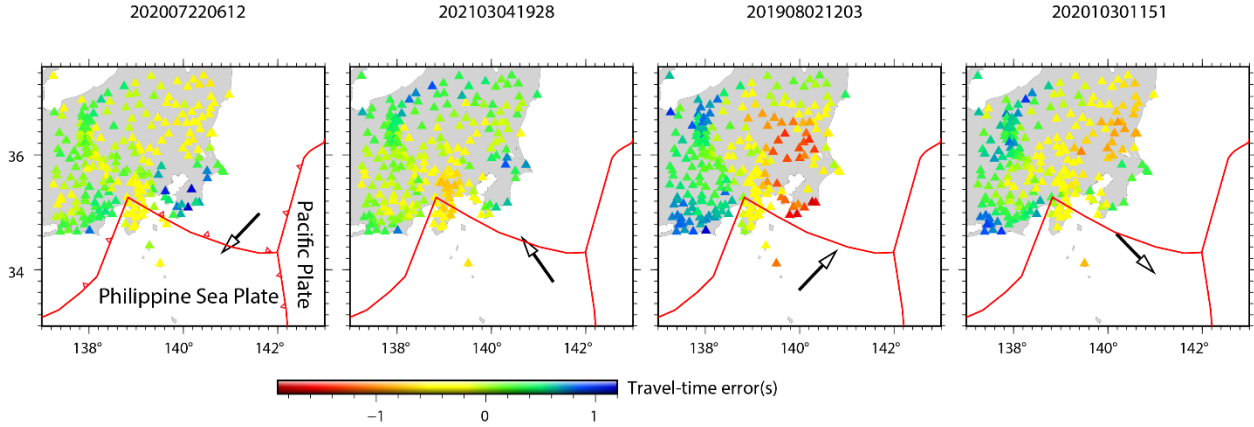


Figure 11. Travel-time errors relative to IASPI model in and around the Kantō plain for events from four different azimuths, as indicated by arrows. The title of each subfigure is the event-id defined by the time of the earthquake.

In our proposed travel-time calibration strategy, two main factors may bring uncertainties into the BP results. The first is how the travel-time error variation deviates from the linear assumption. As stated in Fan and Shearer (2017), if the perturbation of source-side velocity structure is sufficiently random, the corresponding travel-time error varies randomly and the calibration using after-

shock/foreshock may not work. After a ramp removed in the observed travel-time error (e.g., Figure 2h), the residual travel-time error distribution is featured with a mix of random variation and some higher order complexities. One way to further improve the travel-time correction is to use a high-order polynomial (i.e., a curved surface) to fit the travel-time error when there are sufficient data and the influence from the origin time error of calibration events can be isolated or minimized. This process also requires more expensive computational cost. As we use 1D velocity model here as a reference, another way to mitigate the higher order complexity in the travel-time error is to use a 3D global/local velocity model as the reference model. This, however, requires a good regional or global velocity model which is rarely available. Another source of uncertainty may be originated from the inaccurate location of calibration events. This uncertainty can be reduced with a more accurate catalog or relocating calibration events. We do not consider this issue in the current study, because the horizontal location of calibration events should be quite accurate (e.g., uncertainty of a few km) in Japan and Denali where local seismic array is quite dense. In this study, we estimate the location uncertainty in BP results for the mainshock as the average difference between BP inferred locations of medium size earthquakes in the source region and their catalog locations. We use the difference as a uniform uncertainty for all the high frequency radiators. This is clearly a simplified way for location uncertainty estimation. With denser local array and finer regional velocity model, the estimation of uncertainties and the error of BP results will be gradually improved.

We would also like to point out the difference between our travel-time calibration strategy and that proposed by Meng *et al.* (2016) and Zhang (2019). In Meng *et al.* (2016)'s study, they assumed the travel-time error varies linearly along the horizontal ray path (HRP) connecting the main-shock epicenter and a receiver, and projected all the other grid points on the HRP to interpolate travel-time errors (Figure 12a). Here we use a simple scenario (Figure 12b) to show that such calibration may not be appropriate when the calibration event is located further away from the rupture. In this scenario (Figure 12b), the interpolated travel-time error for location  $S$  is equal with that from the epicenter ( $e$ ) if we assume Meng *et al.* (2016)'s strategy. In reality (e.g., Figure 2d-f), it would be a rare coincidence that the HRP is parallel to the gradient direction that of the travel-time error. In another path calibration strategy proposed by Zhang (2019), a 2D interpolation was used to derive travel-time corrections. The 2D interpolation in Zhang (2019) is similar to what we propose here, However, a ridge regression algorithm was adopted in Zhang (2019) to establish travel-time corrections. We do not apply complicate regressions in our strategy because the influence of origin time errors may be not clear, and these regressions may be initial-value sensitive. We show a simple scenario in Figure S3 to illustrate the advantage of linear algorithm over a complicated algorithm.

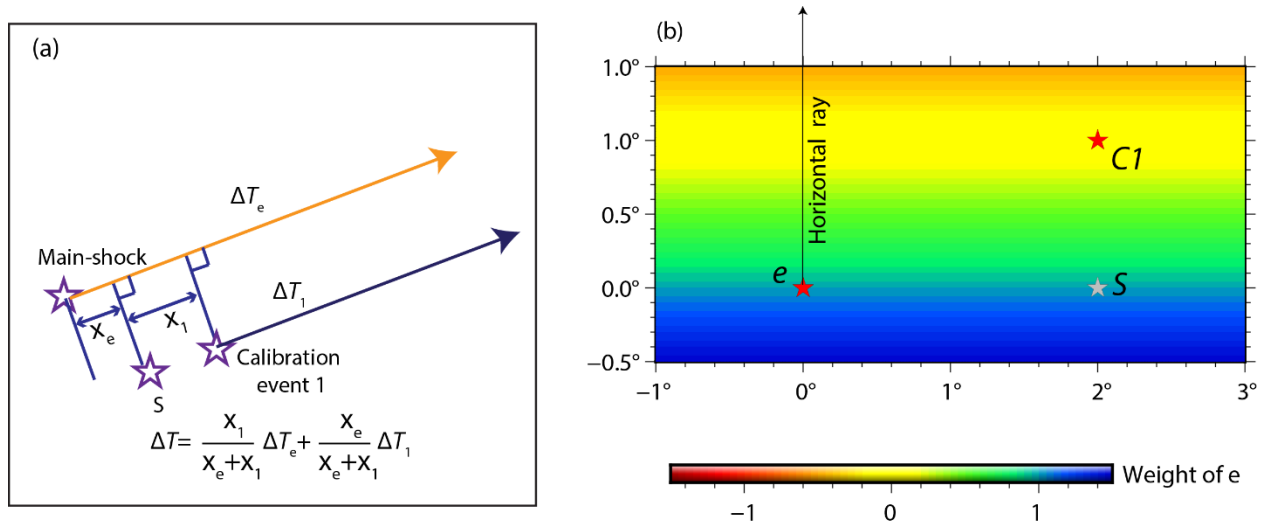


Figure 12. (a) A cartoon illustrating the interpolation method used in Meng *et al.* (2016). (b) An example of the weight (the term  $\frac{x_e}{x_e+x_1}$  in (a)) distribution of the main-shock travel-error. The  $e$  refers to the epicenter of the main-shock and  $C1$  is one of the calibration events. The weight of  $e$  is color coded, where negative and greater than 1 values represent extrapolation and 0 - 1 values mean interpolation. The horizontal ray path are indicated by the arrows.  $S$  is a representative location which is closer to  $C1$  but the estimated travel-time correction is exactly the same as that from  $e$ .

## 5.2 The Denali Earthquake

The aftershocks distribution of the Denali earthquakes and its relationship with the BP results deserve further discussion. The early aftershocks may be triggered by the dynamical stress field generated by the main rupture (e.g., (Kilb *et al.*, 2000)) and therefore their distribution may reflect the specific super-shear dynamic stress field. We show the distribution of the first week aftershocks in histograms as a function of distance to the main fault (Figure 13). Here we divide the DF and TF into four segments based on the BP result and fault segmentation (Figure 13a, b). Segment 1 is corresponding to the super-shear transition and is associated with very few aftershocks, consistent with the proposed signature of a shrunk off-fault damage zone in the transition from sub-Rayleigh to super-shear rupture (e.g., (Okubo *et al.*, 2019, Jara *et al.*, 2021)). Segments 2 and 3 show many more aftershocks and are featured with asymmetric distribution, with more aftershocks located to the southwest of the DF (the extensional side of the rupture), suggesting that more off-fault structures were activated there. Numerical simulations (e.g., (Okubo *et al.*, 2019)) and laboratory experiments (e.g., (Griffith *et al.*, 2009, Aben *et al.*, 2020)) also show that the dynamic stress mainly generate off-fault damages (mainly opening, Mode-I cracks) in the extensional side of a mode II (i.e., strike-slip) rupture. Compared with the after-

shocks around segment 3, in both relative and absolute senses, more aftershocks around segment 2 are located to the northeast of the fault (the compressional stress quadrant of the rupture). This difference could be ascribed to the difference in rupture speeds of the two segments. A rupture speed approaching the P wave velocity leads to a strong Mach cone which attenuates very slowly around the fault, while a rupture speed around  $\sqrt{2}C_s$  results in a weaker Mach cone located around the nodal direction of S waves (Rosakis, 2002, Mello *et al.*, 2014, Mello *et al.*, 2016). We further notice that the envelop of the north side seismicity (around the PS10 station) is likely mirroring the Mach cone shape of the super-shear rupture. Indeed, if we estimate the angle ( $\theta$ ) between the Mach cone and the fault trace we find it to be  $\sim 37^\circ$ , suggesting a rupture speed of ( $V_r = \frac{C_s}{\sin(\theta)}$ )  $1.66 C_S$  (5.5 km/s) which is consistent with that from the BP and near-field strong motion data analyses.

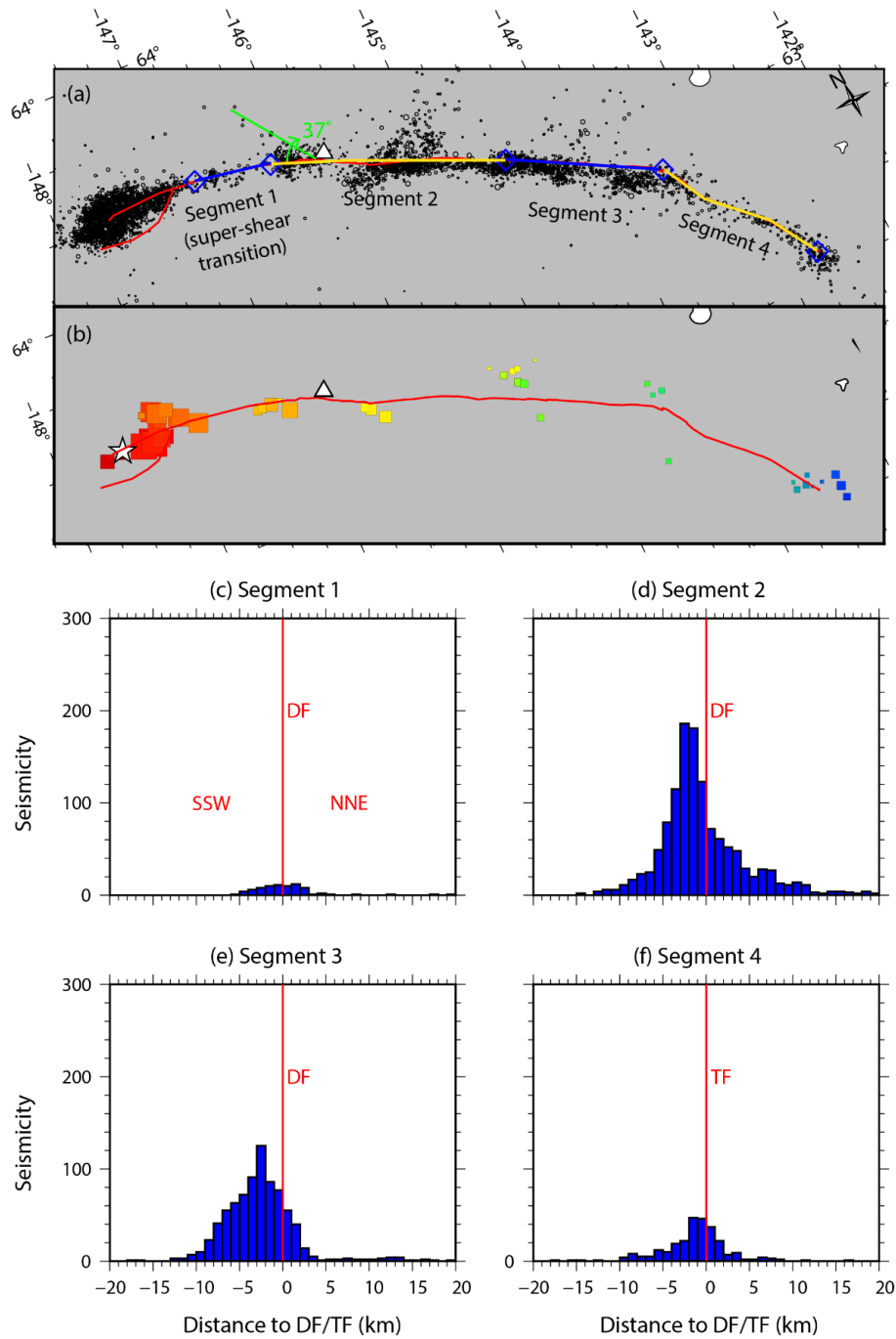


Figure 13 (a) One-week aftershocks following the main-shock. Red lines are surface traces, the blue line is the approximated surface trace used to calculate

the distance of aftershocks to the main rupture, blue diamonds together with the blue line are used to show how we divide the corresponding faults into four segments (blue texts), and the green line is the envelop of seismicity in NNE around segment one. (b) BP result as shown in Figure 8a. (b-e) Histograms of aftershocks' distance to the main fault in the four segments.

Another striking feature of segments 2 and 3 is that although most of the seismicity are located to the southwest of and quite near to the fault, some of the seismicity extends quite far away from the fault to the northeast (Figure 13a). Besides an explanation that there are more remote active faults to the northeastern side, an alternative interpretation is that the southwestern side aftershocks were mainly activated by the stress associated with the rupture tip while the further northeastern side aftershocks were induced by the intense Mach cone as it sweeps that area. This conclusion has been supported by recent modeling the off-fault damage generated by super-shear ruptures (Bhat *et al.*, 2007, Jara *et al.*, 2021). However, further numerical simulations, laboratory experiments, field observations, as well as aftershocks studies may be needed to better understand whether such aftershock distribution is a feature primarily associated with super-shear rupture.

## Conclusion

In the study, we observe that the travel-time error varied linearly in both inland and subduction regions in the dimension ( $\sim 300$  km) of large ruptures. To improve the BP performance, we propose a novel path calibration strategy using earthquakes nearby the target event by linearly interpolating travel-time errors. We demonstrate that such path calibration strategy can better resolve the rupture process of large earthquakes. The successful application of the path-calibrated BP method to the Denali earthquake suggests that the Denali earthquake ruptured at super-shear speeds on both the Denali and Totschunda faults. The consistency between the BP result and the surface trace as well as lab experiments and near-field strong motion analysis based on fracture mechanics, provides strong validation to the BP prediction. We recommend reconciling interdisciplinary observations and analysis should be applied to other case studies wherever conditions allow.

## Acknowledgement

The figures in the paper are plotted using the Generic Mapping Tools (GMT) (Wessel *et al.*, 2019). The seismic data used here are downloaded using the Standing Order for Data (SOD) (Owens *et al.*, 2004) from IRIS and the python package, HinetPy (10.5281/zenodo.4599566) from NEIC. The seismic waveforms are processed using the SAC (Goldstein and Snoke, 2005) and the python package, AIMBAT (Lou *et al.*, 2013). Authors thank USGS and JMA for the earthquake information used in the paper. The project benefits from discussion with Dr. Judith Hubbard and Dr. Thorne Lay. This work is supported by Singapore MOE project (MOE2019-T2-1-182). This work comprises EOS contribution number XXX. Ares Rosakis also wishes to acknowledge the support provided

by NTU, through his Nanyang Visiting Professorship Appointment, in enabling this interdisciplinary collaboration.

## References

- Aagaard, B.T. & Heaton, T.H., 2004. Near-source ground motions from simulations of sustained intersonic and supersonic fault ruptures, *B Seismol Soc Am*, 94, 2064-2078.
- Aben, F.M., Brantut, N. & Mitchell, T.M., 2020. Off-Fault Damage Characterization During and After Experimental Quasi-Static and Dynamic Rupture in Crustal Rock From Laboratory P Wave Tomography and Microstructures, *Journal of Geophysical Research: Solid Earth*, 125, e2020JB019860.
- Asano, K., Iwata, T. & Irikura, K., 2005. Estimation of source rupture process and strong ground motion simulation of the 2002 Denali, Alaska, earthquake, *B Seismol Soc Am*, 95, 1701-1715.
- Avouac, J.P., Meng, L.S., Wei, S.J., Wang, T. & Ampuero, J.P., 2015. Lower edge of locked Main Himalayan Thrust unzipped by the 2015 Gorkha earthquake, *Nat Geosci*, 8, 708-+.
- Baize, S., Nurminen, F., Sarmiento, A., Dawson, T., Takao, M., Scotti, O., Azuma, T., Boncio, P., Champenois, J. & Cinti, F.R., 2020. A worldwide and Unified Database of Surface Ruptures (SURE) for fault displacement hazard analyses, *Seismol Res Lett*, 91, 499-520.
- Bhat, H.S., Dmowska, R., King, G.C., Klinger, Y. & Rice, J.R., 2007. Off-fault damage patterns due to supershear ruptures with application to the 2001 Mw 8.1 Kokoxili (Kunlun) Tibet earthquake, *Journal of Geophysical Research: Solid Earth*, 112.
- Bhat, H.S., Dmowska, R., Rice, J.R. & Kame, N., 2004. Dynamic slip transfer from the Denali to Totschunda faults, Alaska: Testing theory for fault branching, *B Seismol Soc Am*, 94, S202-S213.
- Brocher, T.M., Fuis, G.S., Lutter, W.J., Christensen, N.I. & Ratchkovski, N.A., 2004. Seismic velocity models for the Denali fault zone along the Richardson Highway, Alaska, *B Seismol Soc Am*, 94, S85-S106.
- Dunham, E.M. & Archuleta, R.J., 2004. Evidence for a supershear transient during the 2002 Denali fault earthquake, *B Seismol Soc Am*, 94, S256-S268.
- Dunham, E.M., Favreau, P. & Carlson, J., 2003. A supershear transition mechanism for cracks, *Science*, 299, 1557-1559.
- Eberhart-Phillips, D., Haeussler, P.J., Freymueller, J.T., Frankel, A.D., Rubin, C.M., Craw, P., Ratchkovski, N.A., Anderson, G., Carver, G.A. & Crone, A.J., 2003. The 2002 Denali fault earthquake, Alaska: A large magnitude, slip-partitioned event, *Science*, 300, 1113-1118.
- Ellsworth, W., Celebi, M., Evans, J., Jensen, E., Kayen, R., Metz, M., Nyman, D., Roddick, J., Spudich, P. & Stephens, C., 2004. Near-field ground motion of the 2002 Denali fault, Alaska, earthquake recorded at pump station 10, *Earthquake spectra*, 20, 597-615.
- Fan, W.Y. & Shearer, P.M., 2017. Investigation of Backprojection Uncertainties With M6 Earthquakes, *J Geophys Res-Sol Ea*, 122, 7966-7986.
- Frankel, A., 2004. Rupture process of the M 7.9 Denali fault, Alaska, earthquake: subevents, directivity, and scaling of high-frequency ground motions, *B Seismol Soc Am*, 94, S234-S255.
- Goldstein, P. & Snoke, A., 2005. SAC availability for the IRIS community, *Incorporated Research Institutions for Seismology Newsletter*, 7.
- Griffith, W.A., Rosakis, A., Pollard, D.D. & Ko, C.W., 2009. Dynamic rupture experiments elucidate tensile crack development during propagating earthquake ruptures, *Geology*, 37, 795-798.
- Haeussler, P.J., Schwartz, D.P., Dawson, T.E., Stenner,

H.D., Lienkaemper, J.J., Sherrod, B., Cinti, F.R., Montone, P., Craw, P.A. & Crone, A.J., 2004. Surface rupture and slip distribution of the Denali and Totschunda faults in the 3 November 2002 M 7.9 earthquake, Alaska, *B Seismol Soc Am*, 94, S23-S52.

Hreinsdóttir, S., Freymueller, J.T., Bürgmann, R. & Mitchell, J., 2006. Coseismic deformation of the 2002 Denali fault earthquake: Insights from GPS measurements, *Journal of Geophysical Research: Solid Earth*, 111.

Ishii, M., Shearer, P.M., Houston, H. & Vidale, J.E., 2005. Extent, duration and speed of the 2004 Sumatra-Andaman earthquake imaged by the Hi-Net array, *Nature*, 435, 933-936.

Ishii, M., Shearer, P.M., Houston, H. & Vidale, J.E., 2007. Teleseismic P wave imaging of the 26 December 2004 Sumatra-Andaman and 28 March 2005 Sumatra earthquake ruptures using the Hi-net array, *J Geophys Res-Sol Ea*, 112.

Jara, J., Bruhat, L., Thomas, M.Y., Antoine, S.L., Okubo, K., Rougier, E., Rosakis, A.J., Sammis, C.G., Klinger, Y. & Jolivet, R., 2021. Signature of transition to supershear rupture speed in the coseismic off-fault damage zone, *Proceedings of the Royal Society A*, 477, 20210364.

Ji, C., Helmberger, D.V. & Wald, D.J., 2004. A teleseismic study of the 2002 Denali fault, Alaska, earthquake and implications for rapid strong-motion estimation, *Earthquake Spectra*, 20, 617-637.

Kame, N., Rice, J.R. & Dmowska, R., 2003. Effects of prestress state and rupture velocity on dynamic fault branching, *Journal of Geophysical Research: Solid Earth*, 108.

Kilb, D., Gombert, J. & Bodin, P., 2000. Triggering of earthquake aftershocks by dynamic stresses, *Nature*, 408, 570-574.

Klinger, Y., Choi, J.H. & Vallage, A., 2017. Fault branching and long-term earthquake rupture scenario for strike-slip earthquakes, *Fault zone dynamic processes: Evolution of fault properties during seismic rupture*, 217-228.

Kruger, F. & Ohrnberger, M., 2005. Spatio-temporal source characteristics of the 26 December 2004 Sumatra earthquake as imaged by teleseismic broadband arrays, *Geophysical Research Letters*, 32.

Liao, B.-Y. & Huang, H.-C., 2008. Rupture process of the 2002 M w 7.9 Denali earthquake, Alaska, using a newly devised hybrid blind deconvolution method, *B Seismol Soc Am*, 98, 162-179.

Liu, Z., Song, C., Meng, L., Ge, Z., Huang, Q. & Wu, Q., 2017. Utilizing a 3D global P-wave tomography model to improve backprojection imaging: A case study of the 2015 Nepal earthquake, *B Seismol Soc Am*, 107, 2459-2466.

Lou, X.T., van der Lee, S. & Lloyd, S., 2013. AIMBAT: A Python/Matplotlib Tool for Measuring Teleseismic Arrival Times, *Seismol Res Lett*, 84, 85-93.

Mello, M., Bhat, H., Rosakis, A. & Kanamori, H., 2014. Reproducing the supershear portion of the 2002 Denali earthquake rupture in laboratory, *Earth and Planetary Science Letters*, 387, 89-96.

Mello, M., Bhat, H.S. & Rosakis, A.J., 2016. Spatiotemporal properties of Sub-Rayleigh and supershear rupture velocity fields: Theory and experiments, *Journal of the Mechanics and Physics of Solids*, 93, 153-181.

Meng, L.S., Inbal, A. & Ampuero, J.-P., 2011. A window into the complexity of the dynamic rupture of the 2011 Mw 9 Tohoku-Oki earthquake, *Geophysical Research Letters*, 38, n/a-n/a.

Meng, L.S., Zhang, A.L. & Yagi, Y.J., 2016. Improving back projection imaging with a novel physics-based aftershock calibration approach: A case study of the 2015 Gorkha earthquake, *Geophysical Research Letters*, 43, 628-636.

Oglesby, D.D., Dreger, D.S., Harris, R.A., Ratchkovski, N. & Hansen, R., 2004. Inverse kinematic and forward dynamic

models of the 2002 Denali fault earthquake, Alaska, *B Seismol Soc Am*, 94, S214-S233. Okubo, K., Bhat, H.S., Rougier, E., Marty, S., Schubnel, A., Lei, Z., Knight, E.E. & Klinger, Y., 2019. Dynamics, radiation, and overall energy budget of earthquake rupture with coseismic off-fault damage, *Journal of Geophysical Research: Solid Earth*, 124, 11771-11801. Owens, T.J., Crotwell, H.P., Groves, C. & Oliver-Paul, P., 2004. SOD: Standing order for data, *Seismol Res Lett*, 75, 515-520. Ozacar, A.A. & Beck, S.L., 2004. The 2002 Denali fault and 2001 Kunlun fault earthquakes: complex rupture processes of two large strike-slip events, *B Seismol Soc Am*, 94, S278-S292. Palo, M., Tilmann, F., Krüger, F., Ehlert, L. & Lange, D., 2014. High-frequency seismic radiation from Maule earthquake (Mw 8.8, 2010 February 27) inferred from high-resolution backprojection analysis, *Geophys J Int*, 199, 1058-1077. Ratchkovski, N., Hansen, R., Stachnik, J., Cox, T., Fox, O., Rao, L., Clark, E., Lafevers, M., Estes, S. & MacCormack, J., 2003. Aftershock sequence of the Mw 7.9 Denali fault, Alaska, earthquake of 3 November 2002 from regional seismic network data, *Seismol Res Lett*, 74, 743-752. Rosakis, A., Rubino, V. & Lapusta, N., 2020. Recent milestones in unraveling the full-field structure of dynamic shear cracks and fault ruptures in real-time: From photoelasticity to ultrahigh-speed digital image correlation, *Journal of Applied Mechanics*, 87, 030801. Rosakis, A., Samudrala, O. & Coker, D., 1999. Cracks faster than the shear wave speed, *Science*, 284, 1337-1340. Rosakis, A.J., 2002. Intersonic shear cracks and fault ruptures, *Advances in physics*, 51, 1189-1257. Rosakis, A.J., Xia, K., Lykotrafitis, G. & Kanamori, H., 2007. 4.08 - Dynamic Shear Rupture in Frictional Interfaces: Speeds, Directionality, and Modes. in *Treatise on Geophysics (Second Edition)*, pp. 183-213, ed. Schubert, G. Elsevier, Oxford. Rousseau, C.E. & Rosakis, A.J., 2003. On the influence of fault bends on the growth of sub-Rayleigh and intersonic dynamic shear ruptures, *Journal of Geophysical Research: Solid Earth*, 108. Schwartz, D.P., Haeussler, P.J., Seitz, G.G. & Dawson, T.E., 2012. Why the 2002 Denali fault rupture propagated onto the Totschunda fault: Implications for fault branching and seismic hazards, *Journal of Geophysical Research: Solid Earth*, 117. Simons, M., Minson, S.E., Sladen, A., Ortega, F., Jiang, J., Owen, S.E., Meng, L.S., Ampuero, J.P., Wei, S., Chu, R., Helmberger, D.V., Kanamori, H., Hetland, E., Moore, A.W. & Webb, F.H., 2011. The 2011 magnitude 9.0 Tohoku-Oki earthquake: mosaicking the megathrust from seconds to centuries, *Science*, 332, 1421-1425. Snieder, R. & Sambridge, M., 1992. Ray perturbation theory for traveltimes and ray paths in 3-D heterogeneous media, *Geophys J Int*, 109, 294-322. Templeton, E.L., Baudet, A., Bhat, H.S., Dmowska, R., Rice, J.R., Rosakis, A.J. & Rousseau, C.E., 2009. Finite element simulations of dynamic shear rupture experiments and dynamic path selection along kinked and branched faults, *Journal of Geophysical Research: Solid Earth*, 114. Walker, K.T. & Shearer, P.M., 2009. Illuminating the near-sonic rupture velocities of the intracontinental Kokoxili Mw 7.8 and Denali fault Mw 7.9 strike-slip earthquakes with global P wave back projection imaging, *Journal of Geophysical Research: Solid Earth*, 114. Wang, D., Mori, J. & Koketsu, K., 2016. Fast rupture propagation for large strike-slip earthquakes, *Earth and Planetary Science Letters*, 440, 115-126. Weng, H., Huang, J. & Yang, H., 2015. Barrier-induced

supershear ruptures on a slip-weakening fault, *Geophysical Research Letters*, 42, 4824-4832. Wessel, P., Luis, J., Uieda, L., Scharroo, R., Wobbe, F., Smith, W. & Tian, D., 2019. The generic mapping tools version 6, *Geochemistry, Geophysics, Geosystems*, 20, 5556-5564. Xia, K., Rosakis, A.J. & Kanamori, H., 2004. Laboratory earthquakes: The sub-Rayleigh-to-supershear rupture transition, *Science*, 303, 1859-1861. Yagi, Y., Nakao, A. & Kasahara, A., 2012. Smooth and rapid slip near the Japan Trench during the 2011 Tohoku-oki earthquake revealed by a hybrid back-projection method, *Earth and Planetary Science Letters*, 355, 94-101. Yao, H., Gerstoft, P., Shearer, P.M. & Mecklenbräuker, C., 2011. Compressive sensing of the Tohoku-Oki Mw 9.0 earthquake: Frequency-dependent rupture modes, *Geophysical Research Letters*, 38, n/a-n/a. Yin, J., Yang, H., Yao, H. and Weng, H., 2016. Coseismic radiation and stress drop during the 2015 Mw 8.3 Illapel, Chile megathrust earthquake. *Geophysical Research Letters*, 43(4), pp.1520-1528. Zeng, H., Wei, S. & Wu, W., 2020. Sources of uncertainties and artefacts in back-projection results, *Geophys J Int*, 220, 876-891. Zhang, A., 2019. *Theories and Applications of Enhanced Earthquake Back-projection Imaging*, edn, Vol., pp. Pages, eScholarship, University of California.